PHYSICAL REVIEW D **86,** 094503 (2012)

Chiral transition and $U(1)_A$ symmetry restoration from lattice QCD using domain wall fermions

A. Bazavov,[1] Tanmoy Bhattacharya,[2] Michael I. Buchoff,[3] Michael Cheng,[3,*] N. H. Christ,[4] H.-T. Ding,[1] Rajan Gupta,[2] Prasad Hegde,[1] Chulwoo Jung,[1] F. Karsch,[1,5] Zhongjie Lin,[4] R. D. Mawhinney,[4] Swagato Mukherjee,[1] P. Petreczky,[1] R. A. Soltz,[2] P. M. Vranas,[3] and Hantao Yin[4]

(HotQCD Collaboration)

[1]*Physics Department, Brookhaven National Laboratory, Upton, New York 11973, USA*
[2]*Theoretical Division, Los Alamos National Laboratory, Los Alamos, New Mexico 87545, USA*
[3]*Physics Division, Lawrence Livermore National Laboratory, Livermore, California 94550, USA*
[4]*Physics Department, Columbia University, New York, New York 10027, USA*
[5]*Fakultät für Physik, Universität Bielefeld, D-33615 Bielefeld, Germany*
(Received 26 June 2012; published 6 November 2012)

We present results on both the restoration of the spontaneously broken chiral symmetry and the effective restoration of the anomalously broken $U(1)_A$ symmetry in finite temperature QCD at zero chemical potential using lattice QCD. We employ domain wall fermions on lattices with fixed temporal extent $N_\tau = 8$ and spatial extent $N_\sigma = 16$ in a temperature range of $T = 139$–195 MeV, corresponding to lattice spacings of $a \approx 0.12$–0.18 fm. In these calculations, we include two degenerate light quarks and a strange quark at fixed pion mass $m_\pi = 200$ MeV. The strange quark mass is set near its physical value. We also present results from a second set of finite temperature gauge configurations at the same volume and temporal extent with slightly heavier pion mass. To study chiral symmetry restoration, we calculate the chiral condensate, the disconnected chiral susceptibility, and susceptibilities in several meson channels of different quantum numbers. To study $U(1)_A$ restoration, we calculate spatial correlators in the scalar and pseudoscalar channels, as well as the corresponding susceptibilities. Furthermore, we also show results for the eigenvalue spectrum of the Dirac operator as a function of temperature, which can be connected to both $U(1)_A$ and chiral symmetry restoration via Banks-Casher relations.

DOI: 10.1103/PhysRevD.86.094503 PACS numbers: 11.15.Ha, 12.38.Gc

I. INTRODUCTION

In the limit of vanishing up and down quark masses, quantum chromodynamics (QCD) possesses a chiral $SU(2)_L \times SU(2)_R$ symmetry. However, the QCD vacuum does not respect this symmetry. Instead the nonvanishing vacuum expectation value of the $SU(2)_L \times SU(2)_R$ non-invariant operators $\bar{\psi}_l \psi_l$, for $l = u, d$ reflect a smaller, $SU(2)_V$ vacuum symmetry. This symmetry-breaking vacuum order is expected to disappear at high temperature implying a phase transition separating a low-temperature chirally asymmetric phase from a high-temperature phase with restored chiral symmetry. The chirally symmetric, high-temperature phase of QCD was present during the evolution of the early universe and is also expected to be created in heavy-ion collision experiments. Thus, studies of chiral symmetry restoration at high temperatures are of great physical importance.

At the classical level QCD possesses an additional $U(1)_A$ symmetry which is broken by the axial anomaly. This results in both the anomalous term in the conservation law for the $U(1)_A$ axial current of Adler [1] and Bell and Jackiw [2] as well as 't Hooft's explicit violation of the global symmetry [3] arising from fermion zero modes associated with topologically nontrivial gauge-field configurations. At low temperatures this anomalous $U(1)_A$ symmetry is also broken by the QCD vacuum. However, above the QCD phase transition vacuum symmetry breaking has disappeared and the effects of the axial anomaly can be studied directly.

Lattice QCD is ideally suited to study these symmetries and their degree of restoration with increasing temperature. However, such studies are complicated by the fermion doubling problem. This fundamental difficulty, present in any discrete theory of fermions, sharply reduces the chiral symmetry that is present in a lattice fermion formulation. The Wilson formulation shows chiral symmetry only in the continuum limit. Staggered fermions are more successful and preserve a single, nonanomalous $U(1)$ axial symmetry at finite lattice spacing.

In this paper, we employ the domain wall fermion (DWF) formulation of Kaplan [4] and Shamir [5] which, at the classical level, shows the full $SU(2)_L \times SU(2)_R \times U(1)_A$ symmetry, with lattice symmetry breaking controlled by the size, L_s, of an additional fifth dimension.

*Current address: Center for Computational Science, Boston University, Boston, MA 02215, USA.

For the results reported here L_s varies between 32 and 96 and is sufficiently large that the residual quark mass induced by lattice effects is on the order of 10 MeV or smaller–sufficiently small that its effects can be easily incorporated as an additive shift in the quark mass. Most previous lattice studies of the chiral transition in QCD use staggered fermions, for which the issue of anomalous symmetry is somewhat subtle, involving possible noncommutativity of the continuum and chiral limits and the nonunitarity of the rooted theory at finite lattice spacing [6–10]. In contrast, the DWF formulation possesses an easily understood anomalous $U(1)_A$ symmetry [5], broken by the same topological effects which produce anomalous symmetry breaking in the continuum, with explicit lattice artifacts appearing at order $m_{\rm res}a^2$. Thus, the degree of anomalous symmetry restoration with increasing temperature is a natural focus of this paper.

At sufficiently high temperatures anomalous $U(1)_A$ symmetry breaking can be studied using the dilute instanton gas approximation [11]. In this approximation one finds exponential suppression of the instanton density as the gauge coupling decreases so that the $U(1)_A$ symmetry becomes exact in the limit $T \rightarrow \infty$. When the dilute instanton gas approximation is justified, the $U(1)_A$ symmetry-breaking effects it predicts are very small. With decreasing temperature, the semiclassical approximation underlying the dilute instanton gas picture becomes unreliable and the degree of anomalous symmetry breaking becomes a nonperturbative question well suited to a DWF lattice study. While one might imagine that anomalous $U(1)_A$ breaking remains small as the temperature decreases from asymptotically large values, even down to the critical temperature, T_c, it is also possible that new, nonperturbative phenomena emerge at lower temperatures leading to a significant topological charge density and to large $U(1)_A$ symmetry breaking.

The degree of $U(1)_A$ symmetry breaking may have interesting physical consequences. For example, if the $U(1)_A$ breaking is sufficiently large near the phase transition for QCD with two massless flavors then this transition can be second order, belonging to the three-dimensional $O(4)$ universality class [12,13]. On the other hand, if the axial symmetry breaking is negligible then this $O(4)$ universality class is no longer appropriate for the larger symmetry of the long-distance variables and the chiral transition is expected to be first order [12,13], although in this case a second-order transition is also allowed with a different symmetry-breaking pattern, $U(2)_L \times U(2)_R/U(2)_V$ [14]. Hence, the nature of the chiral phase transition itself may depend critically on the strength of the $U(1)_A$ symmetry breaking.

In heavy-ion collision experiments, it may also be possible to observe signatures of $U(1)_A$ symmetry restoration through measurements of low-mass dileptons [15]. Moreover, an effective restoration of the axial $U(1)_A$ symmetry above T_c may lead to softening of the η' mass resulting in interesting experimental signatures [16–18]. In fact, recently it has been claimed that the results from the Relativistic Heavy-Ion Collider (RHIC) suggest softening of the η' mass indicating partial restoration of the $U(1)_A$ symmetry in hot and dense matter [19]. Hence, studies related to $U(1)_A$ symmetry restoration with increasing temperature have important theoretical and phenomenological consequences.

As discussed above, chiral symmetry restoration, as well as the degree of $U(1)_A$ symmetry breaking above T_c, are essentially nonperturbative in nature. At present, lattice QCD, as the most reliable nonperturbative technique, is ideally suited for such studies. In fact, extensive lattice QCD studies of chiral symmetry restoration have been carried out. For a review and summary of recent lattice QCD results see Refs. [20,21]. Most of these lattice studies have been performed using staggered fermion discretization schemes. Staggered fermions have also been used to study the degree of axial symmetry restoration in high-temperature QCD [22–26]. However, as described earlier, for staggered fermions at nonzero lattice spacing, chiral symmetry, the axial anomaly and its relation to the index theorem suffer from significant complications. Thus, a study using the DWF discretization scheme, which preserves the full $SU(2)_L \times SU(2)_R$ symmetry and reproduces the correct anomaly even for nonzero values of lattice spacing, is well motivated. To date, there have been only a few fully dynamical calculations using chiral fermion formulations—domain wall fermions [27,28] and overlap fermions [29].

In this paper we study the chiral transition and degree of restoration of $U(1)_A$ symmetry for $T \geq T_c$ by performing lattice QCD simulations using the DWF action with two degenerate light (up and down) and one heavier (strange) quarks. We employ lattices with spatial size $N_\sigma = 16$ and temporal extent $N_\tau = 8$, with lattice spacings in the range $a \approx 0.12$–0.18 fm, corresponding to a temperature range of $T = 137$–198 MeV. We work on a line of constant physics, i.e., the strange quark mass is fixed to near its physical value, while for most of the results presented here the two light-quark masses have been chosen so that $m_\pi \approx 200$ MeV. This extends earlier studies of the QCD transition with domain wall fermions [27,28] by going to a lighter quark mass, using a gauge action optimized for the relatively large lattice spacing needed for such an $N_\tau = 8$ study, and exploring in more detail the chiral aspects of the QCD transition. We also present a thorough study of the eigenvalue spectrum of the Dirac operator employing a variant of the method of Giusti and Lüscher [30] to convert the spectrum of the Hermitian DWF Dirac operator to a spectrum evaluated in the $\overline{\rm MS}$ scheme which has a well-defined continuum limit. This allows us to examine the density of eigenvalues near zero as a function of temperature. This density can be directly related to both

$SU(2)_L \times SU(2)_R$ and $U(1)_A$ breaking and restoration through Banks-Casher type formulas.

This paper is organized as follows. We start in Sec. II with a discussion of the setup of our lattice calculation, including the choice of lattice action and the determination of the line of constant physics. In Sec. III we present details of our eigenvalue calculations with DWF, including the methods used to convert the low-lying eigenvalue spectrum of the Hermitian DWF Dirac operator to a spectrum meaningful in the continuum limit. In Sec. IV we introduce the basic observables which we will use to explore the chiral aspects of the QCD transition, emphasizing the role of the $U(1)_A$ symmetry for the transition. Section V examines the restoration of $SU(2)_L \times SU(2)_R$ chiral symmetry through the subtracted chiral condensate, disconnected chiral susceptibility, and vector and axial vector screening masses. Section VI deals with the restoration of $U(1)_A$ symmetry by examining the scalar and pseudoscalar screening correlators, their respective susceptibilities, and their relation to the topological charge. We discuss our results and give conclusions in Sec. VII. Appendix A gives further details on the normalization of the eigenvalue spectrum, Appendix B discusses the renormalization of the disconnected, staggered chiral susceptibility, while Appendix C gives the details of the evolution algorithms used to generate our gauge-field ensembles. Finally, Appendix D examines a discrepancy between the topological and disconnected $\bar{\psi}\gamma^5\psi$ susceptibilities and concludes that the combination of APE smearing and improved gauge-field operator [31] used here to determine the topological charge contains large lattice artifacts when applied at nonzero temperatures on the coarse ensembles studied in this paper.

II. CALCULATION DETAILS

A. Fermion and gauge action

For this calculation, we use the domain wall fermion action. At the lattice spacings at which we work, i.e., those appropriate to study the finite temperature transition region with temporal extent $N_\tau = 8$, the residual chiral symmetry breaking, parameterized by the residual mass $m_{\rm res}$, becomes quite large because of the proliferation of localized topology-changing dislocations in the gauge field. This leads to eigenstates of the five-dimensional transfer matrix with unit eigenvalue, mixing the left- and right-handed chiral modes [5,32]. Because $m_{\rm res}$ acts as an additive renormalization to the quark mass, a large $m_{\rm res}$ makes it difficult to explore the transition region with a reasonably small pion mass.

In this paper, we have used two different approaches to reduce the residual chiral symmetry breaking. The first is to choose a large value for the size of the fifth dimension, $L_s = 96$. This is coupled with judicious choices for the input quark masses, m_l and m_s so that the *total* quark masses, i.e. $(m_l + m_{\rm res})$ and $(m_s + m_{\rm res})$, are fixed in lattice units. (Throughout this paper we will express dimensional quantities in lattice units unless physical units are explicitly specified.) This results in pion masses of $m_\pi \approx 225$–275 MeV in the transition region. However, because $m_{\rm res}$ only falls linearly with L_s in this regime ($m_\pi \sim 1/\sqrt{L_s}$), it is computationally very costly to perform calculations at small m_π by simply increasing L_s [32].

An alternative to increasing L_s is to directly suppress the localized modes which are the primary contribution to $m_{\rm res}$ at coarse lattice spacings. This is done by augmenting our action with a ratio of determinants of the twisted-mass Wilson Dirac operator. This determinant ratio, which we call the "Dislocation Suppressing Determinant Ratio" (DSDR), suppresses those gauge-field configurations which contribute most to the mixing between left- and right-handed walls. This method is a further development of earlier applications of the 4D Wilson fermion determinant for this purpose with both domain wall and overlap fermions [33–35].

For both approaches with and without the DSDR method, we employ the Iwasaki gauge action [36] for the gauge links. The Iwasaki gauge action has been used extensively in zero-temperature calculations coupled with domain wall fermions [37–40]. The RBC-UKQCD collaboration has also begun a large-scale study of zero-temperature physics using the Iwasaki gauge action and the DSDR method. Zero-temperature results with the DSDR method have been presented in [41–43].

B. Dislocation suppressing determinant ratio

To lowest order in a^2, the residual chiral symmetry breaking caused by the finite extent in the fifth dimension acts as an additive renormalization to the bare quark mass. This additive renormalization is known as the residual mass $m_{\rm res}$. At fixed bare coupling, the dependence of $m_{\rm res}$ on the extent of the fifth direction L_s can be parametrized as [32]

$$m_{\rm res} = c_1 \rho_H(\lambda_c) \frac{e^{-\lambda_c L_s}}{L_s} + c_2 \rho_H(0) \frac{1}{L_s}, \qquad (1)$$

where $\rho_H(\lambda)$ represents the density of eigenmodes of the effective 4D Hamiltonian $\mathcal{H} = -\log(\mathcal{T})$, where $\mathcal{T}$ is the transfer matrix in the fifth direction that controls the mixing of chiral modes between the 4D boundaries. The 4D Hamiltonian, $\mathcal{H}$ is closely related to the Hermitian Wilson operator, $H_W = \gamma^5 D_W(-M_5)$, via $\mathcal{H} = 2\tanh^{-1}(H_W/(2 + D_W))$, and it has been shown that the zero modes of $\mathcal{H}$ and H_W coincide [5].

The first term in Eq. (1) represents contributions from eigenmodes with eigenvalues λ greater than the mobility edge, λ_c. These modes have extended 4D support and their contributions to $m_{\rm res}$ are exponentially suppressed with L_s. The second term corresponds to contributions from near-zero eigenmodes of the 4D Hamiltonian, or equivalently eigenmodes where the 5D transfer matrix $\mathcal{T}$ is near unity,

thus allowing nearly unsuppressed mixing of the domain walls in the fifth direction. These near-zero eigenmodes come largely from localized dislocations in the gauge field corresponding to topology change [44–46]. At strong coupling, gauge-field dislocations rapidly become more common, so that the dominant contribution to $m_{\rm res}$ comes from the near-zero eigenmodes of $\mathcal{H}$ and the second, power-suppressed term in Eq. (1).

One method to reduce the large residual chiral symmetry breaking is to augment the gauge action with the determinant of the 4D Hermitian Wilson Dirac operator, $H_W(-M_5) = \gamma^5 D_W(-M_5)$ [33–35], where M_5 is the domain wall height ($M_5 = 1.8$ in our calculation). Including this determinant as a factor in the path integral explicitly suppresses those configurations which have a small eigenvalue of H_W, and thus also those configurations with near-zero modes of $\mathcal{H}$.

Unfortunately, the suppression of the zero modes of H_W also suppresses exactly those configurations that change topology during a molecular dynamics evolution. Therefore, in order to allow for the correct sampling of all topological sectors, we augment the Wilson Dirac operator with a chirally twisted mass,

$$D_W(-M_5) \rightarrow D_W(-M_5 + i\epsilon\gamma^5). \tag{2}$$

We then employ the following weighting factor on the gauge fields:

$$\mathcal{W}(M_5, \epsilon_b, \epsilon_f) = \frac{\det[D_W^\dagger(-M_5 + i\epsilon_f\gamma^5)D_W(-M_5 + i\epsilon_f\gamma^5)]}{\det[D_W^\dagger(-M_5 + i\epsilon_b\gamma^5)D_W(-M_5 + i\epsilon_b\gamma^5)]} = \frac{\det[D_W^\dagger(-M_5)D_W(-M_5) + \epsilon_f^2]}{\det[D_W^\dagger(-M_5)D_W(-M_5) + \epsilon_b^2]}. \tag{3}$$

The bosonic and fermionic "twisted-mass" parameters ϵ_b, ϵ_f can be tuned so that gauge-field topology changes during hybrid Monte Carlo (HMC) evolution, but the localized dislocations which contribute to the residual mass are suppressed. We call the weighting factor $\mathcal{W}(M_5, \epsilon_b, \epsilon_f)$ the dislocation suppressing determinant ratio (DSDR). Employing this ratio of determinants ensures that the ultraviolet modes of the theory are minimally affected so that bare parameters such as β and the quark masses do not shift significantly compared to those used with the standard domain wall fermion action.

C. Lattice ensembles

1. $L_s = 96$ ensembles

The finite temperature ensembles that we generated with $L_s = 96$ all have spatial volume of 16^3 and temporal extent $N_t = 8$. We generated nine different lattice ensembles for temperatures in the range $T \in [137, 198]$ MeV. The bare couplings $\beta \in [1.965, 2.10]$ span approximately the same range used in a previous study of the transition region with domain wall fermions with $L_s = 32$ by the RBC-Bielefeld Collaboration [28]. Since the only change in the lattice action on these ensembles is the choice of the size of the fifth dimension, to leading order this mainly affects residual chiral symmetry breaking and has a minimal effect on the bare coupling and the lattice cutoff. We therefore use the same interpolation as in [28] to determine the temperatures of each of our lattice ensembles.

The input light and strange quark masses, m_l and m_s, are chosen so that the total quark masses, including the contributions from the residual mass, are given by $m_l + m_{\rm res} = 0.00675$ and $m_s + m_{\rm res} = 0.045$. However, these quark masses are not along a line of constant physics. At $\beta = 2.025$, we can directly compare our quark masses with the determination of m_π in [28]. Our choice gives $m_\pi \approx 250$ MeV. The choice of a fixed bare light-quark mass implies that m_π in physical units will vary across the set of bare couplings that we use. The change in temperature from $\beta = 2.025$ to the extremal points in our range suggests a 10% variation for m_π in either direction. This gives a range of $m_\pi \in [225, 275]$ MeV, with m_π being heavier at higher temperatures.

Table I gives the details for these ensembles.

2. DSDR ensembles

For the gauge action augmented with DSDR, we generated several ensembles at zero temperature ($N_\tau = 32$, $N_\sigma = 16$) in order to determine the bare couplings and quark masses appropriate for exploring the transition region at $N_\tau = 8$. For the twisted-mass coefficients in the

TABLE I. Summary of the $16^3 \times 8$, $L_s = 96$ finite temperature ensembles without DSDR. The total molecular dynamics time per trajectory is $\tau = 0.5$. Quark masses were chosen so that the $m_l + m_{\rm res} \approx 0.00675$ and $m_s + m_{\rm res} \approx 0.045$. Residual masses are estimated from those reported in Ref. [28] assuming $m_{\rm res} \sim 1/L_s$ scaling. Note here and in the following all dimensional quantities are expressed in lattice units unless other physical units are specified.

T (MeV)	β	m_l	m_s	$m_{\rm res}$	Trajectory
137	1.965	0.00045	0.0387	0.0063	1720
146	1.9875	0.00245	0.0407	0.0043	1640
151	2.00	0.00325	0.0415	0.0035	1540
156	2.0125	0.00395	0.0422	0.0028	1465
162	2.025	0.00435	0.0426	0.0024	1835
167	2.0375	0.00485	0.0431	0.0019	1690
173	2.05	0.00525	0.0435	0.0015	1570
188	2.08	0.00585	0.0441	0.0009	2006
198	2.10	0.00585	0.0441	0.0006	1648

determinant ratio, we found that the choice of $\epsilon_f = 0.02$ and $\epsilon_b = 0.5$ allows for a reasonable rate of tunneling between topological sectors while still suppressing residual chiral symmetry breaking [41]. At two values of the coupling, $\beta = 1.70$ and 1.82 we generated ensembles with two different quark masses, corresponding to $m_\pi \approx 300$, 400 MeV, respectively.

We have also used preliminary results from the RBC-UKQCD calculation with $N_\sigma = 32$, $N_\tau = 64$ at $\beta = 1.75$ to provide a better interpolation for the bare parameters of our finite temperature ensembles.

At finite temperature, we produced ensembles at seven different temperatures in the range 139 MeV $\leq T \leq$ 195 MeV with $N_\tau = 8$ and spatial extent $N_\sigma = 16$. The quark masses are chosen so that the physical pion masses are fixed, $m_\pi \approx 200$ MeV, while the strange quark mass, m_s, is chosen so that $(m_l + m_{\rm res})/(m_s + m_{\rm res}) = 0.088$, close to its physical value. Table II summarizes the parameters for both our finite and zero-temperature ensembles. Appendix C gives the details of the various evolution algorithms used to generate these ensembles.

Except for the $T = 139$, 149 MeV ensembles, we use $L_s = 32$ for the extent of the fifth dimension. Because of the rapid growth of the residual mass as one moves to stronger coupling, the use of a negative input light-quark mass becomes necessary at the lowest temperatures so that the total light-quark mass $m_{\rm tot} = m_l + m_{\rm res}$ corresponds to a fixed physical pion mass, $m_\pi \approx 200$ MeV.

In principle, the presence of a negative quark mass admits the possibility for a singular fermion matrix, resulting in "exceptional configurations" that destroy the reliability of the calculation. However, the residual chiral symmetry breaking in our calculation produces a dynamically generated mass $m_{\rm res}$ that additively renormalizes our quark masses, theoretically moving one away from any singularities in the fermion matrix. Of course, $m_{\rm res}$ is only well defined when one considers an ensemble average, so if one uses a negative quark mass that is too large, i.e., $|m_l| \sim m_{\rm res}$, fluctuations in the gauge configurations may induce the unwanted singularities even if $m_{\rm tot} > 0$.

For $T = 139$ MeV, we initially used a negative light-quark mass of $m_l = -0.00786$, with $m_{\rm res} \approx 0.013$ at $L_s = 32$. It was quickly discovered that this resulted in a singular fermion matrix, signaled by the nonconvergence of the conjugate gradient inversion. As a result, we switched to $L_s = 48$ at this temperature, where a smaller, but still negative light quark $m_l = -0.00136$ could be used to achieve the desired total light-quark mass. At $L_s = 48$, we saw no exceptional configurations in our ensemble.

At $T = 149$ MeV we produced configurations at both $L_s = 32$ and $L_s = 48$ in order to verify that the use of a negative input quark mass had no effect on physical observables, beyond small $O(a^2)$ effects. With $L_s = 32$, a negative input quark mass, $m_l = -0.00189$, is used, while at $L_s = 48$, we have $m_l = 0.00173$. Both of these ensembles (ensembles 2 and 3 in Table II) correspond to approximately the same physical pion mass, $m_\pi \approx 200$ MeV. We did not see any large differences between these two ensembles in quantities such as the disconnected chiral susceptibility, renormalization coefficients, or eigenvalue

TABLE II. Summary of zero and finite temperature ensembles with DSDR. Each lattice ensemble is given a label for later reference. The total molecular dynamics time per trajectory is $\tau = 1.0$. The residual mass, $m_{\rm res}$ and the average plaquette ($\langle U_\Box \rangle$) are also tabulated.

Finite Temperature Ensembles											
Label	T (MeV)	β	N_σ	N_τ	L_s	m_l	m_s	$m_{\rm res}$	m_π (MeV)	Trajectory	$\langle U_\Box \rangle$
1	139(6)	1.633	16	8	48	−0.00136	0.0519	0.00588(39)	191(7)	2996	0.46913(8)
2	149(5)	1.671	16	8	32	−0.00189	0.0464	0.00643(9)	199(5)	6000	0.48491(3)
3	149(5)	1.671	16	8	48	0.00173	0.0500	0.00295(3)	202(5)	7000	0.48407(2)
4	159(4)	1.707	16	8	32	0.000551	0.0449	0.00377(11)	202(3)	3659	0.49777(4)
5	168(4)	1.740	16	8	32	0.00175	0.0427	0.00209(9)	197(2)	3343	0.50912(4)
6	177(4)	1.771	16	8	32	0.00232	0.0403	0.00132(6)	198(2)	3540	0.51916(4)
7	186(5)	1.801	16	8	32	0.00258	0.0379	0.00076(3)	195(3)	4715	0.52845(3)
8	195(6)	1.829	16	8	32	0.00265	0.0357	0.00047(1)	194(4)	6991	0.53672(3)
Zero-temperature ensembles											
9	···	1.70	16	32	32	0.013	0.047	0.00420(2)	394(9)	1360	0.49510(3)
10	···	1.70	16	32	32	0.006	0.047	0.00408(6)	303(7)	1200	0.49509(3)
11	···	1.75	16	16	32	0.006	0.037	0.00188	-	1255	0.51222(3)
12	···	1.75[a]	32	64	32	0.0042	0.045	0.00180(5)	246(5)	1288	0.512203(7)
13	···	1.75[a]	32	64	32	0.001	0.045	0.00180(5)	172(4)	1560	0.512235(7)
14	···	1.82	16	32	32	0.013	0.040	0.00062(2)	398(9)	2235	0.53384(1)
15	···	1.82	16	32	32	0.007	0.040	0.00063(2)	304(7)	2134	0.53386(2)

[a]The values given for $\beta = 1.75$ are zero-temperature results from RBC-UKQCD [42,43].

TABLE III. Results for r_0, m_ρ, m_π, and the lattice scale, a^{-1}. At each value of β, we perform simple linear extrapolations to $m_l = -m_{\rm res}$, i.e., the chiral limit, for r_0 and m_ρ. The lattice scale is fixed using the extrapolated value for r_0.

Label	β	m_l	r_0	m_ρ	m_π	$1/a$ [a] (GeV)
9	1.70	0.013	2.895(11)	0.68(2)	0.310(1)	···
10		0.006	2.992(27)	0.67(2)	0.238(1)	···
Extrapolated		−0.0040	3.13(7)	0.66(6)	···	1.27(4)
12	1.75	0.0042	3.349(20)	0.57(2)	0.1810(3)	···
13		0.0010	3.356(22)	0.56(2)	0.1264(3)	···
Extrapolated		−0.0018	3.36(4)	0.56(4)	···	1.36(3)
14	1.82	0.013	3.743(28)	0.56(2)	0.255(2)	···
15		0.007	3.779(37)	0.53(2)	0.195(2)	···
Extrapolated		−0.00064	3.83(9)	0.49(5)	···	1.55(5)

[a]Lattice scale determined using $r_0 = 0.487(9)$ fm.

spectrum. However, in the chiral condensate we did see a significant difference in the two ensembles, presumably caused by the difference in the leading-order ultraviolet divergent m_l/a^2 term that enters in the calculation of the chiral condensate on the lattice. Table II also shows a 0.2% difference in the average plaquette value, as we should expect from the small change in the fermion determinant caused by the increase in L_s from 32 to 48. (Recall that the ratio of the physical fermion to Pauli-Villars DWF determinants should have an $L_s \to \infty$ limit.)

D. Line of constant physics

As discussed in the preceding subsection, the $L_s = 96$ ensembles do not lie on a line of constant physics, but rather a line of constant bare quark mass. This results in the pion mass changing from $m_\pi \approx 225$ MeV at the lowest temperature in our ensemble to $m_\pi \approx 275$ MeV at the highest temperature.

For the DSDR ensembles, we have endeavored to move along a line of fixed physical pion mass, $m_\pi = 200$ MeV. Table III summarizes our results for m_π, m_ρ, and r_0 on the zero-temperature ensembles.

In order to determine the lattice scale, we have used the Sommer parameter r_0, determined from the static quark potential. The quantity r_0, extrapolated to the chiral limit, can be related to the lattice scale using its physical value $r_0 = 0.487(9)$ fm, determined using domain wall fermions [40]. The temperature is given by $T = 1/N_\tau a$. The values for r_0/a in Table III allow us to determine the bare couplings needed for finite temperature lattice ensembles in the transition region.

To describe $T(\beta)$ in physical units, we use a modified form of the two-loop renormalization group running, which includes an extra term for the $\mathcal{O}(a^2)$ lattice artifacts:

$$T(\beta) = \frac{1}{N_\tau a(\beta)} = (c_0 + c_1 \hat{a}^2(\beta)) \frac{1}{\hat{a}(\beta)}, \tag{4}$$

$$\hat{a}(\beta) = \exp\left(-\frac{\beta}{12 b_0}\right)\left(\frac{6 b_0}{\beta}\right)^{-b_1/(2b_0^2)}; \qquad b_0 = \frac{9}{(4\pi)^2}; \qquad b_1 = \frac{64}{(4\pi)^4}, \tag{5}$$

where $\hat{a}(\beta)$ is the continuum two-loop renormalization-group (RG) running for the lattice spacing. The left panel

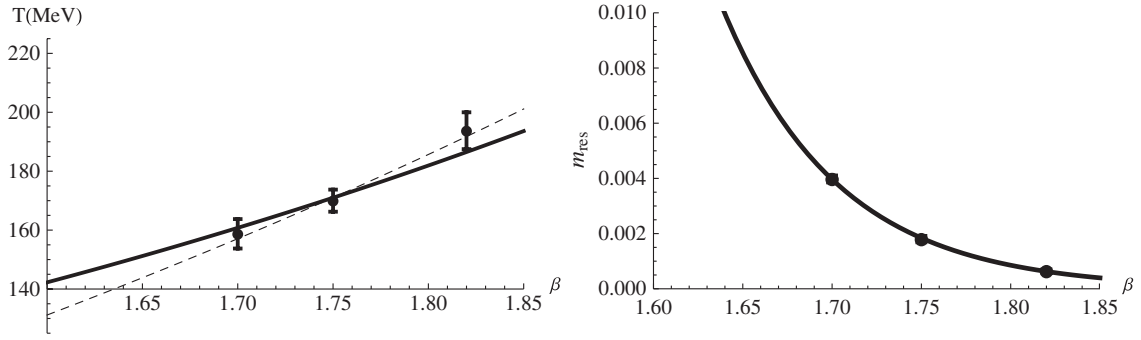

FIG. 1. Left panel: temperature for $N_\tau = 8$ is plotted versus β. The solid curve is the fit to the continuum RG running; $c_0 = 25.2(3)$ MeV. The dashed curve is the result of the fit to Eq. (4) which includes an added a^2 correction; $c_0 = 29.7(2.9)$ MeV, $c_1 = -204(132)$ MeV. Right panel: $m_{\rm res}a$ is plotted versus β with an exponential fit: $m_{\rm res}(\beta) = A\exp(-B\beta)$; $A = 8.7(9.7) \times 10^8$, $B = 15.4(6)$.

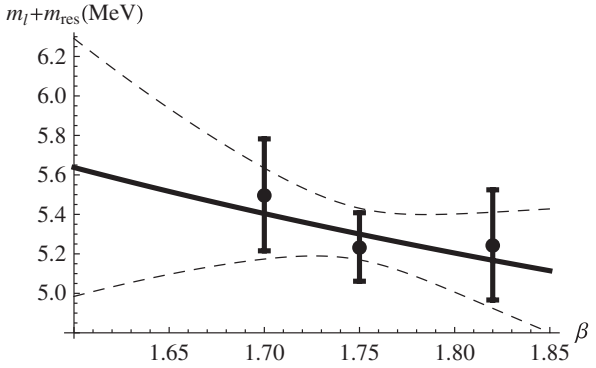

FIG. 2. Total light-quark mass for $m_\pi = 200$ MeV line of constant physics, with a fit to the lattice-corrected mass anomalous dimension. Dashed curves represent the 1-σ error band.

of Fig. 1 shows the result of the fit of the β dependence of the temperature to both the lattice-corrected RG fit of Eq. (4), and to the continuum RG running, i.e., the case where $c_1 = 0$. As can be seen, the lattice-corrected fit provides a better description of the data.

The zero-temperature ensembles show that the residual mass is strongly dependent on the lattice spacing. At coarser lattice spacings, the aforementioned dislocations are more common and cause $m_{\rm res}$ to increase rapidly as one moves from high to low temperature. The right panel of Fig. 1 shows $m_{\rm res}$ as a function of β. We find that a simple exponential Ansatz describes the data well.

Finally, to ensure that we simulate along a line of fixed pion mass, we must account for the running of the bare quark masses as the bare coupling is changed. Since the residual chiral symmetry-breaking results in an additive shift in the quark mass, to leading order in chiral perturbation theory, the pion mass depends on the total quark mass, $m_{\rm tot} = m_l + m_{\rm res}$, as

$$m_\pi^2 \propto (m_l + m_{\rm res}).$$

This linear quark mass dependence is a surprisingly good description of earlier data [40] and sufficiently accurate for the present purpose.

This allows us to determine the bare quark masses required for a specific line of constant physics on the zero-temperature ensembles listed in Table III. Figure 2 shows the quark masses required for $m_\pi = 200$ MeV. We also fit these results for $m_{\rm tot}(\beta)$ to the lattice-corrected two-loop running of the mass anomalous dimension:

$$m_{\rm tot} \equiv (m_l + m_{\rm res}) = (A + B\hat{a}^2(\beta))\left(\frac{12b_0}{\beta}\right)^{4/9}. \quad (6)$$

The lattice-corrected fit provides a good interpolation that allows us to achieve a line of constant physics on the finite temperature ensembles.

III. DETERMINING THE DIRAC EIGENVALUE SPECTRUM

The spectrum of eigenvalues of the Hermitian Dirac operator provides important insight into the physics of QCD. The Dirac spectrum depends dramatically on the temperature and is fundamentally connected with both spontaneous and anomalous chiral symmetry breaking. These topics will be explored in detail in later sections of this paper.

In this section we will explain how the continuum Dirac spectrum can be determined from the spectrum of the five-dimensional DWF Dirac operator, including a method to determine its normalization. The Ritz method used to determine the lowest 100 eigenvalues for each of our finite temperature ensembles will then be briefly described as well as the numerical details of our determination of the normalization of those eigenvalues. A derivation for this normalization method, following the approach of Giusti and Lüscher [30], is given in Appendix A. The resulting Dirac eigenvalue spectrum, computed and normalized following the methods described in this section, will be presented and analyzed in Sec. VI, in an effort to determine the temperature dependence and the origin of anomalous $U(1)_A$ symmetry breaking.

A. Relating the continuum and DWF Dirac spectrum

The domain wall fermion formulation can be viewed as a five-dimensional theory whose low energy properties accurately reproduce four-dimensional QCD. All low energy Green's functions and matrix elements are expected to agree with those of a four-dimensional theory and it is only at high momenta or short distances that the five-dimensional character of the theory becomes visible. This perspective applies also to the five-dimensional DWF Dirac operator whose small eigenvalues and corresponding eigenstates should closely approximate those of a continuum four-dimensional theory. This can be shown explicitly for the free theory, order by order in perturbation theory and by direct numerical evaluation in lattice QCD. With the exception of gauge configurations which represent changing topology, the modes with small eigenvalues are literally four dimensional with support concentrated on the four-dimensional left and right walls of the original five-dimensional space.

Thus, we can learn about the continuum Dirac eigenvalue spectrum by directly studying that of the DWF Dirac operator, $D^{\rm DWF}$, as defined by Eqs. (1)–(3) in Ref. [47]. Of course, just as with other regulated versions of the continuum theory, explicit renormalization is needed to convert from a bare to a renormalized eigenvalue density. Because the continuum Dirac operator, $\not{\partial} + m$, is linear in the quark mass, we should expect the Dirac eigenvalues to be related between different renormalization schemes by the same factor Z_m that connects the masses. If we have two regularized theories which describe the same long-distance

physics with bare masses m and $m' = Z_{m\to m'}m$, then we should expect that their eigenvalue densities would be related by

$$\rho'(\lambda') = \frac{1}{Z_{m\to m'}}\rho(\lambda'/Z_{m\to m'}). \tag{7}$$

Note this expectation is consistent with the form of the Banks-Casher relation, $\langle\bar{\psi}\psi\rangle = \pi\rho(0)$, as the equality of the mass term in equivalent theories requires $\langle\bar{\psi}'\psi'\rangle = \langle\bar{\psi}\psi\rangle/Z_{m\to m'}$.

The renormalization of the bare input quark mass, m_f, for DWF has been extensively studied and the factor $Z_{m_f\to\overline{\rm MS}}(\mu^2)$ needed to convert this input bare mass to a continuum, $\overline{\rm MS}$ value at the scale μ is accurately known [40]. However, in contrast to the continuum theory or staggered or Wilson lattice fermions, the input quark mass for DWF does not enter as an additive constant but instead appears as a coupling strength between the two four-dimensional walls. Thus, for DWF the Dirac spectrum and the quark mass will in general be related to their continuum counterparts by *different* renormalization factors. To properly renormalize the DWF Dirac spectrum we should begin with the Hermitian operator $\gamma^5 R_5 D^{\rm DWF}$ and then add the identity operator multiplied by the parameter $m_{\rm tw}$:

$$\gamma^5 R_5 D^{\rm DWF} + m_{\rm tw} = \gamma^5 R_5 (D^{\rm DWF} + \gamma^5 R_5 m_{\rm tw}). \tag{8}$$

Here R_5 performs a simple reflection in the fifth dimension, taking the point (x, s) to the point $(x, L_s - 1 - s)$, where x is the space-time coordinate and $0 \le s \le L_s - 1$ the coordinate in the fifth dimension. The renormalization factor, $Z_{\rm tw\to\overline{MS}}$, needed to convert the DWF spectrum to the continuum, $\overline{\rm MS}$ spectrum then relates this new DWF pseudoscalar operator to the corresponding $\overline{\rm MS}$ continuum operator:

$$(\bar{\psi}(x)\gamma^5\psi(x))^{\overline{\rm MS}} \approx \frac{1}{Z_{\rm tw\to\overline{MS}}}\sum_{s=0}^{L_s-1}\bar{\Psi}(x, s)\gamma^5\Psi(x, L_s - 1 - s), \tag{9}$$

where $\Psi(x, s)$ is the five-dimensional DWF field. These two operators, which appear in different theories, are equated in Eq. (9) in the sense that they give the same matrix elements when inserted in corresponding long-distance Green's functions.

It is convenient to determine the renormalization constant $Z_{\rm tw\to\overline{MS}}$ in two steps. In the first we determine the constant $Z_{{\rm tw}\to m_f}$ which relates this reflected pseudoscalar term and the standard pseudoscalar term belonging to the same chiral representation as the usual DWF mass term $\bar{\psi}\psi$:

$$\bar{\psi}(x)\gamma^5\psi(x) = \frac{1}{Z_{{\rm tw}\to m_f}}\bar{\Psi}(x)R_5\gamma^5\Psi(x), \tag{10}$$

where the operator on the right-hand side is the same as that in the right-hand side of Eq. (9) with the explicit sum over the s coordinate suppressed.

Then in the second step we perform the well-understood conversion between the standard DWF mass operator and a continuum, $\overline{\rm MS}$ normalized mass operator using $Z_{m_f\to\overline{\rm MS}}$:

$$Z_{\rm tw\to\overline{MS}} = Z_{m_f\to\overline{\rm MS}}Z_{{\rm tw}\to m_f}. \tag{11}$$

After the first step, we can compare the eigenvalue density $\rho(\lambda)$ for the lattice DWF operator with the usual lattice result for the chiral condensate using the Banks-Casher relation,

$$\langle\bar{\psi}\psi\rangle = \frac{\pi}{Z_{{\rm tw}\to m_f}}\rho(0), \tag{12}$$

since both the left- and right-hand sides now use the same bare normalization conventions. In the second step we are simply dividing both sides of Eq. (12) by the common factor $Z_{m_f\to\overline{\rm MS}}$ to convert from lattice to $\overline{\rm MS}$ normalization.

B. Calculation of $Z_{tw\to m_f}$

Because the operators $\bar{\psi}(x)\gamma^5\psi(x)$ and $\bar{\Psi}(x)R_5\gamma^5\Psi(x)/Z_{{\rm tw}\to m_f}$ are supposed to be equivalent at long distances, we can determine the needed factor $Z_{{\rm tw}\to m_f}$ by simply taking the ratio of equivalent Green's functions, evaluated at distances greater than the lattice spacing a, containing these two operators:

$$Z_{{\rm tw}\to m_f} = \frac{\langle O_1 \ldots O_n\bar{\Psi}(x)R_5\gamma^5\Psi(x)\rangle}{\langle O_1 \ldots O_n\bar{\psi}(x)\gamma^5\psi(x)\rangle}, \tag{13}$$

where the numerator and denominator in this expression are intended to represent identical Green's functions except for the choice of pseudoscalar vertex.

We will now determine $Z_{{\rm tw}\to m_f}$ and test the accuracy to which the ratio given in Eq. (13) defines a unique constant by studying the ratio of two type of matrix elements. In the first we examine simple two-point correlators between each of the pseudoscalar densities in Eq. (13) and the operator $O_\pi(t)$ which creates a pion from a Coulomb gauge fixed wall source located at the time t:

$$\mathcal{R}_\pi(t) = \frac{\langle\sum_{\vec{x}}\bar{\Psi}(\vec{x}, t)R_5\gamma^5\Psi(\vec{x}, t)O_\pi(0)\rangle}{\langle\sum_{\vec{x}}\bar{\psi}(\vec{x}, t)\gamma^5\psi(\vec{x}, t)O_\pi(0)\rangle}, \tag{14}$$

which for large t is the ratio of matrix elements of our two pseudoscalar operators between a pion state and the vacuum. Results are presented in Table IV.

Second, we examine off-shell, three-point Green's functions evaluated in Landau gauge which again contain each of the pseudoscalar densities being compared and a quark and an antiquark field carrying momenta p_1 and p_2, allowing us to see the degree to which the ratio in Eq. (13) does not depend on the small external momenta (MOM) p_1 and p_2:

TABLE IV. Values for the renormalization factor $Z_{\mathrm{tw}\to m_f}$ obtained from the ratio of pseudoscalar correlators $\mathcal{R}_\pi$ defined in Eq. (14).

Label	β	T (MeV)	$\mathcal{R}_\pi$
10	1.70	0	1.774(5)
11	1.75	0	1.570(4)
15	1.82	0	1.397(2)
2	1.671	149	1.905(6)
3	1.671	149	1.980(7)
4	1.707	159	1.725(8)
5	1.740	168	1.631(11)
6	1.771	177	1.476(4)
7	1.801	186	1.439(3)
8	1.829	195	1.365(3)

$$\mathcal{R}_{\mathrm{MOM}}(p_1, p_2) = \frac{\mathrm{Tr}\left\langle \sum_{x_2,x_1} e^{i(p_2x_2-p_1x_1)}\psi(x_2)\bar{\Psi}(0)R_5\gamma^5\Psi(0)\bar{\psi}(x_1)\right\rangle}{\mathrm{Tr}\left\langle \sum_{x_1,x_2} e^{i(p_2x_2-p_1x_1)}\psi(x_2)\bar{\psi}(0)\gamma^5\psi(0),\ \bar{\psi}(x_1)\right\rangle}. \tag{15}$$

Here we are using the well-studied methods of Rome/Southampton nonperturbative renormalization [48] to compare the normalizations of the operators $\bar{\Psi}R_5\gamma^5\Psi$ and $\bar{\psi}\gamma^5\psi$. For a recent application of this method to other operators in a DWF context, see Ref. [49]. For both Eqs. (14) and (15), we expect the ratio to be independent of t and of p_1 and p_2, respectively, and to yield the same value $Z_{\mathrm{tw}\to m_f}$.

When evaluating the momentum space Green's functions in Eq. (15) we generate the needed quark propagators using a series of volume sources [50]. For each specific four-momentum p we evaluate 12 propagators, one for each spin and color, using the sources

$$\eta(x, p)_{\alpha,a;\beta,b} = e^{ip\cdot x}\delta_{\alpha\beta}\delta_{ab}, \tag{16}$$

where α and a are the spin and color indices of the source η while β and b label the spins and colors of the 12 sources evaluated for each four-momentum p. We perform our calculation using both nonexceptional kinematics, $p_1^2 = p_2^2 = (p_1 - p_2)^2$, and exceptional kinematics, $p_1 = p_2$. Results for the ratios $\mathcal{R}^{\mathrm{non-ex}}_{\mathrm{MOM}}(p_1, p_2)$ and $\mathcal{R}^{\mathrm{ex}}_{\mathrm{MOM}}(p_1, p_2)$ for the three zero-temperature ensembles are presented in Table VI and Fig. 3. The specific momentum components used to construct p_1 and p_2 are listed in Table V.

The ratios presented in Tables IV and VI and plotted in Fig. 3 at a given value of β are all expected to equal the common renormalization factor $Z_{\mathrm{tw}\to m_f}$. However, as is evident from these tables and figure, this expectation is realized at only the 20% level, suggesting the presence of significant $O((pa)^2)$ errors and implying a similar uncertainty in

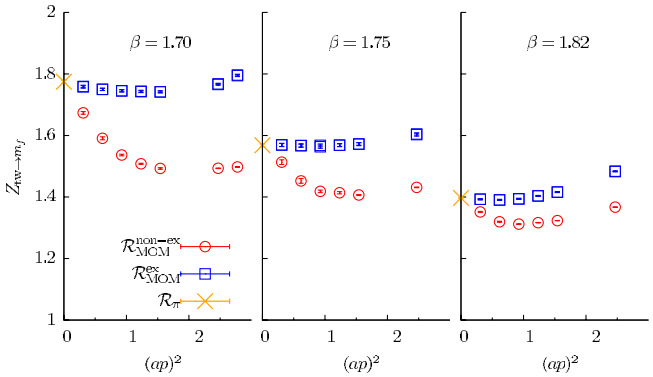

FIG. 3 (color online). Plots of the results for the quantity $Z_{\mathrm{tw}\to m_f}$ given in Tables IV and VI for each of the three values of β that were studied at zero temperature. The single value of $\mathcal{R}_\pi$ is plotted as an "×" in each panel and given the value $(pa)^2 = 0$. (The scale on the leftmost y axis applies to all three plots.) As discussed in the text, the discrepancies between $\mathcal{R}^{\mathrm{non-ex}}_{\mathrm{MOM}}$ and $\mathcal{R}^{\mathrm{non-ex}}_{\mathrm{MOM}}$ are indicative of $O((pa)^2)$ errors, so we use the value of $\mathcal{R}_\pi$ for $Z_{\mathrm{tw}\to m_f}$.

extracting a consistent value for the important quantity $Z_{\mathrm{tw}\to m_f}$. In fact, the behavior of these results is consistent with an $O((pa)^2)$ origin for these discrepancies. The larger dependence on momentum of the nonexceptional ratio $\mathcal{R}^{\mathrm{non-ex}}_{\mathrm{MOM}}(p_1, p_2)$ than seen in $\mathcal{R}^{\mathrm{ex}}_{\mathrm{MOM}}(p_1, p_2)$ and its larger deviation from the more consistent quantities $\mathcal{R}^{\mathrm{ex}}_{\mathrm{MOM}}(p_1, p_2)$ and $\mathcal{R}_\pi$ is reasonable since the nonexceptional kinematics were originally introduced to ensure that large momenta flow everywhere in the corresponding Green's function [49]. The better agreement between the quantities $\mathcal{R}^{\mathrm{ex}}_{\mathrm{MOM}}(p_1, p_2)$ and $\mathcal{R}_\pi$ and the smaller momentum dependence of $\mathcal{R}^{\mathrm{ex}}_{\mathrm{MOM}}(p_1, p_2)$ is also consistent with the smaller internal momenta expected in these Green's functions with exceptional kinematics. Finally, the decreasing differences between these three quantities as β increases from 1.70 to 1.82 with the corresponding decrease in a is also consistent with these violations of universality arising from finite lattice spacing errors.

TABLE V. The components of the two momentum four-vectors p_A and p_B used to compute the quantities $\mathcal{R}_{\mathrm{MOM}}(p_1, p_2)$ given in Table VI. For nonexceptional momenta, we use $p_1 = p_A$ and $p_2 = p_B$, while for exceptional momenta, only a single momentum, either $p_1 = p_2 = p_A$ or $p_1 = p_2 = p_B$ is used. Here $L = 16$ is the spatial size of the lattice.

$(pa)^2$	$p_AL/2\pi$	$p_BL/2\pi$
0.308	(1,1,0,0)	(0,1,1,0)
0.671	(1,1,1,1)	(1, 1, 1, −1)
0.925	(2,1,1,0)	(2, 0, −1, 1)
1.234	(2,2,0,0)	(0,2,2,0)
1.542	(2,2,1,1)	(2, −1, 2, 1)
2.467	(2,2,2,2)	(2, 2, 2, −2)
2.776	(3,2,2,1)	(3, 2, −1, −2)

TABLE VI. Values for the ratio $\mathcal{R}_{\mathrm{MOM}}(p_1, p_2)$ defined in Eq. (15). For nonexceptional momenta, the quantity $\mathcal{R}^{\text{non-ex}}_{\mathrm{MOM}}(p_1 = p_A, p_2 = p_B)$ is shown. For exceptional momenta, the average of $\mathcal{R}^{\text{non-ex}}_{\mathrm{MOM}}(p_1 = p_2 = p_A)$ and $\mathcal{R}^{\text{non-ex}}_{\mathrm{MOM}}(p_1 = p_2 = p_B)$ is shown. The first column shows the value of $(p_1 a)^2 = (p_2 a)^2 = (pa)^2$. Results from 12, 20, and 21 configurations have been averaged to give the values for $\beta = 1.70$, 1.75, and 1.82, respectively. The quark mass values and lattice sizes used for these results are given in Table IV. The significant variation among the results for a given value of β indicate large $O((pa)^2)$ errors.

	$\beta = 1.70$		$\beta = 1.75$		$\beta = 1.82$	
$(pa)^2$	$\mathcal{R}^{\text{non-ex}}_{\mathrm{MOM}}$	$\mathcal{R}^{\text{ex}}_{\mathrm{MOM}}$	$\mathcal{R}^{\text{non-ex}}_{\mathrm{MOM}}$	$\mathcal{R}^{\text{ex}}_{\mathrm{MOM}}$	$\mathcal{R}^{\text{non-ex}}_{\mathrm{MOM}}$	$\mathcal{R}^{\text{ex}}_{\mathrm{MOM}}$
0.308	1.673(5)	1.759(4)	1.507(5)	1.566(4)	1.352(2)	1.393(2)
0.617	1.591(5)	1.745(4)	1.450(5)	1.562(4)	1.320(2)	1.390(2)
0.925	1.536(3)	1.745(3)	1.418(3)	1.562(4)	1.312(1)	1.394(2)
1.234	1.508(2)	1.744(3)	1.412(2)	1.564(4	1.3165(7)	1.404(1)
1.542	1.493(2)	1.742(3)	1.406(1)	1.570(4)	1.3233(6)	1.416(1)
2.467	1.4933(10)	1.766(3)	1.4313(7)	1.613(3)	1.3670(4)	1.484(1)
2.776	1.4977(8)	1.796(3)	-	-	-	-

We therefore adopt the hypothesis that the discrepancies between these different determinations of $Z_{\mathrm{tw}\to m_f}$ arise from finite lattice spacing effects and that the most reliable value for $Z_{\mathrm{tw}\to m_f}$ will be obtained at smallest momentum. Hence, we use the ratio $\mathcal{R}_\pi$ to provide values for $Z_{\mathrm{tw}\to m_f}$. This choice has the additional benefit that we have evaluated this ratio on the finite temperature ensembles allowing us to use $\mathcal{R}_\pi$ to provide values of $Z_{\mathrm{tw}\to m_f}$ for each of our values of β, avoiding extrapolation. Note that the discrepancy between the finite and zero-temperature results for $\mathcal{R}_\pi$ shown in Table IV for the near-by β values $\beta = 1.700, 1.707$ and $\beta = 1.820, 1.829$ indicate remaining systematic a^2 errors in our determination of $Z_{\mathrm{tw}\to m_f}$ that are on the order of 5%.

C. Normalization conventions

Using the methods described above, we can convert our results for the quark mass, chiral condensate, and Dirac spectrum into a single normalization scheme, allowing a meaningful comparison between the eigenvalues in the Dirac spectrum and the corresponding quark mass. We adopt the commonly used $\overline{\mathrm{MS}}$ scheme, normalized at a scale $\mu = 2$ GeV.

We use the DWF results for the continuum, $\mu = 2$ GeV, $\overline{\mathrm{MS}}$ quark masses determined in Ref. [40], $m_s^{\overline{\mathrm{MS}}}(2\ \mathrm{GeV}) = (96.2 \pm 2.7)$ MeV and $m_{ud}^{\overline{\mathrm{MS}}}(2\,\mathrm{GeV}) = (3.59 \pm 0.21)\,\mathrm{MeV}$, and the accurate linear dependence of m_π^2 and m_K^2 on the quark masses in the region studied to convert a lattice light-quark mass, $\tilde{m}_l = m_f + m_{\mathrm{res}}$ corresponding to a pion mass $m_\pi(\tilde{m}_l)$ into this same $\overline{\mathrm{MS}}$ scheme using the relation

$$m_l^{\overline{\mathrm{MS}}}(2\ \mathrm{GeV}) = (3.59 + 96.2)\ \mathrm{MeV}\frac{(m_\pi(\tilde{m}_l))^2}{2(m_K)^2}, \qquad (17)$$

where $m_K = 495$ MeV denotes the physical value of the kaon mass. The renormalization factor is then given by

$$Z_{m_f\to\overline{\mathrm{MS}}} = \frac{99.79\ \mathrm{MeV}}{2\tilde{m}}\left(\frac{m_\pi(\tilde{m}_l)}{495\ \mathrm{MeV}}\right)^2 \qquad (18)$$

for each of our ensembles. Note the lattice quark mass, $\tilde{m}$, substituted in Eq. (18) must be expressed in units of MeV to define a conventional, dimensionless value for $Z_{m_f\to\overline{\mathrm{MS}}}$. The resulting $Z_{m_f\to\overline{\mathrm{MS}}}$ factors for our seven ensembles are given in Table VII.

The factors given in Table VII will also be used to convert values of the chiral condensate $\bar{\psi}\psi$ (when constructed from the usual 4D surface, lattice operators) and Dirac spectrum (when normalized with the same conventions as $\bar{\psi}\psi$) into $\mu = 2$ GeV, $\overline{\mathrm{MS}}$ values according to the relations

$$(\bar{\psi}\psi)^{\overline{\mathrm{MS}}} = \frac{(\bar{\psi}\psi)^{\mathrm{lat}}}{Z_{m_f\to\overline{\mathrm{MS}}}}, \qquad (19)$$

$$\rho(\lambda)^{\overline{\mathrm{MS}}} = \frac{\rho^{\mathrm{lat}}(\lambda/Z_{m_f\to\overline{\mathrm{MS}}})}{Z_{m_f\to\overline{\mathrm{MS}}}}. \qquad (20)$$

Of course, because the quark masses and lattices scales that we use are interpolated and extrapolated from only

TABLE VII. Results for the factors $Z_{m_f\to\overline{\mathrm{MS}}}(2\ \mathrm{GeV})$ which convert a lattice quark mass, $\tilde{m}$ into a mass normalized in the $\overline{\mathrm{MS}}$ conventions at $\mu = 2$ GeV.

Label	T (MeV)	$Z_{m_f\to\overline{\mathrm{MS}}}(2\ \mathrm{GeV})$
1	139	1.47(14)
3	149	1.49(10)
4	159	1.51(7)
5	168	1.53(6)
6	177	1.55(6)
7	186	1.57(7)
8	195	1.58(9)

three zero-temperature ensembles, there is significant uncertainty in our determination of the renormalization factors. However, for the purposes of the present paper, we believe that these renormalization factors in Table VII have sufficient accuracy.

D. Determining DWF Dirac eigenvalues and eigenvectors

We directly diagonalize the five-dimensional Hermitian DWF Dirac operator $D_H = R_5\gamma_5 D^{\mathrm{DWF}}$ using the Kalkreuter-Simma (KS) version of the Ritz method [51]. Details of this method have been described in [47,52].

At each KS iteration, we use the conjugate gradient method to find the lowest N_{eig} eigenvalues of D_H^2 and corresponding eigenvectors one by one, by minimizing the Ritz functional,

$$\mu(\Psi) = \frac{\langle\Psi|D_H^2|\Psi\rangle}{\langle\Psi|\Psi\rangle}. \tag{21}$$

We can then calculate the eigenvalues of D_H by diagonalizing D_H in the subspace spanned by the eigenvectors of D_H^2 previously obtained. The precision of the KS method is controlled by the maximum relative change of all the eigenvalues between each KS iteration.

A spurious eigenmode problem may arise in the Jacobi diagonalization of D_H, if only one of the paired eigenvectors is included in the subspace. The spurious eigenmode's corresponding vector is the linear combination of two almost degenerate eigenvectors with eigenvalues of opposite signs. We resolve this problem by applying D_H to the problematic vector and find the proper linear combination of the resulting vector and the original problematic vector which is the true eigenvector.

Using these methods we have computed the 100 eigenvalues with the smallest magnitude of the DWF Dirac operator on the seven finite temperature ensembles in the temperature range 149 MeV $\leq T \leq$ 195 MeV as well as the $\beta = 1.75$, zero-temperature ensemble discussed below. Table VIII identifies the configurations that were used in these calculations.

TABLE VIII. List of the configurations used in the Dirac spectrum calculation as well as the results for the average smallest normalized eigenvalue ($\mathcal{R}\Lambda_0$). Here N_{start} is the first configuration number on which the spectrum was computed, while N_{cfg} gives the total number of configurations on which the spectrum was determined. In each case these configurations were separated by 5 time units. (The sequence of trajectories used for run #8 contained one anomaly: samples 430 and 431 were separated by three instead of five time units.)

Label	T (MeV)	N_{start}	N_{cfg}	$\mathcal{R}$	$\mathcal{R}\Lambda_0$	$m_l + m_{\mathrm{res}}$
2	149	300	340	1.905	0.00632	0.00459
3	149	300	340	1.980	0.00606	0.00469
4	159	300	408	1.725	0.00828	0.004321
5	168	300	239	1.631	0.01334	0.00384
6	177	300	246	1.476	0.02170	0.00364
7	186	300	374	1.439	0.03131	0.00334
8	195	302	1140	1.365	0.03837	0.00311
11	0	300	252	1.568	0.00489	0.00488

E. Normalized spectral density

The results for the Dirac spectrum at finite temperature obtained using these methods are presented and analyzed in Sec. VI, where the restoration of $U_A(1)$ symmetry is studied. In this section we examine the Dirac spectrum obtained on the zero-temperature ensemble labeled #11, with volume 16^4 and $\beta = 1.75$.

The discussion in the present section has three objectives. First, we explicitly apply the normalization factors to convert the bare eigenvalues of the DWF Dirac operator into the $\overline{\mathrm{MS}}$ scheme. The resulting spectral density is expressed in physical units and can easily be compared with both physical and simulated $\overline{\mathrm{MS}}$ values of the quark masses as well as with the QCD scale, $\Lambda_{\mathrm{QCD}} \sim 300$ MeV. Second, we convert the spectrum of the Hermitian DWF Dirac operator, which includes the effects of the nonzero quark masses to the more conventional spectrum from which the mass has been removed, a step which depends critically on the normalization procedure and is sensitive to finite lattice spacing errors. Finally, we examine the Banks-Casher relation between the resulting spectrum and the chiral condensate.

Figure 4 shows histograms of the Dirac eigenvalues measured on 340 configurations from the zero-temperature, 16^4 ensemble #11 in Table VIII. In the left-hand panel of this figure, the histogram of eigenvalues Λ is obtained by converting the eigenvalues of the lattice DWF Dirac operator, as described above, to the $\overline{\mathrm{MS}}$ scheme with $\mu =$ 2 GeV. On each configuration the 100 eigenvalues of smallest magnitude have been determined. Figure 4 shows histograms of these 34 000 eigenvalues. The rightmost vertical line in both panels identifies the minimum value from the set of the 100th largest eigenvalues on each of the 340 configurations. For eigenvalues less than this "minmax" value the histogram accurately represents the complete spectrum, undistorted by our cutoff of 100 eigenvalues per configuration.

Here, Λ denotes an eigenvalue of the full Hermitian DWF Dirac operator. These eigenvalues include the effect of the quark mass and in the continuum limit would have the form

$$\Lambda = \sqrt{\lambda^2 + \tilde{m}^2}. \tag{22}$$

The left-hand panel of Fig. 4 demonstrates the effect of using a consistent normalization scheme for the quark masses. The two leftmost vertical lines in that plot correspond to the simulated light and strange quark masses, $\tilde{m}_l$ and $\tilde{m}_s$, in the same $\overline{\mathrm{MS}}$ normalization. The expected

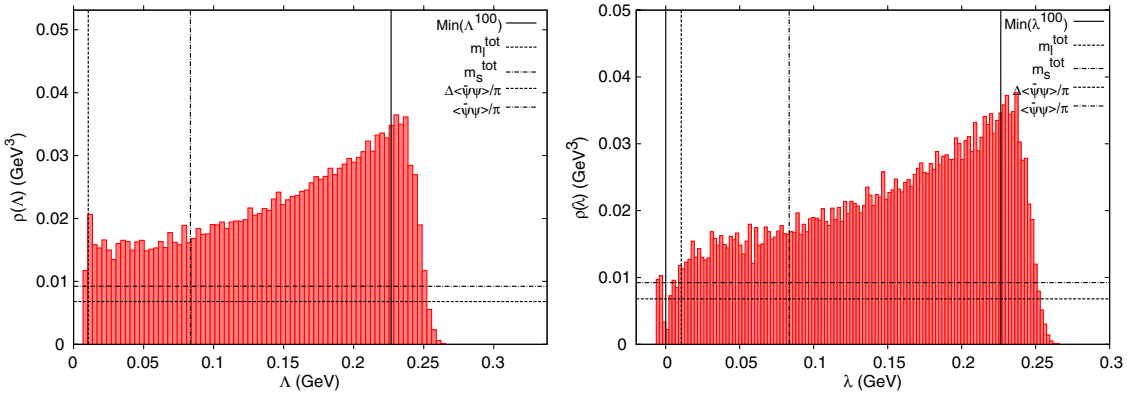

FIG. 4 (color online). Histogram of the spectrum of eigenvalues Λ of the Hermitian DWF Dirac operator normalized in the $\overline{\text{MS}}$ scheme at the scale $\mu = 2$ GeV (left). These eigenvalues are calculated on the zero-temperature ensemble labeled #11. The right-hand panel shows a histogram of the eigenvalues $\lambda = \sqrt{\Lambda^2 - (m_f + m_{\text{res}})^2}$ from which the quark mass has been removed. In this panel, the region $\lambda > 0$ shows those values for which $\Lambda^2 > (m_f + m_{\text{res}})^2$, i.e., λ is purely real, a condition that should be obeyed in the continuum limit. The region $\lambda < 0$ shows those eigenvalues with $\Lambda^2 < (m_f + m_{\text{res}})^2$, i.e., λ pure imaginary, plotted on the negative part of the x axis as $\lambda = -|\sqrt{\Lambda^2 - (m_f + m_{\text{res}})^2}|$. These unphysical values give a visible measure of the finite lattice spacing distortions to the region of small $\lambda > 0$.

coincidence between the peak in the Λ distribution at the smallest eigenvalues and the vertical line representing the light-quark mass occurs only after the relative normalization $\mathcal{R} = 1.570$ from Table VIII between the DWF operator and the conventional input quark mass discussed above has been applied.

In the continuum theory the mass is conventionally removed from the Dirac operator before its eigenvalues are determined so that the usual eigenvalue distribution is given for the quantity λ in Eq. (22). In our case, the transformation to this more usual eigenvalue distribution requires converting each eigenvalue Λ_n into a corresponding $\lambda_n = \sqrt{\Lambda_n^2 - \tilde{m}_l^2}$. Unfortunately, this step is vulnerable to finite lattice spacing effects which allow an occasional value of Λ_n to be smaller than $\tilde{m}_l$, leading to an unphysical, imaginary result for λ_n. This should become increasingly rare in the limit $a \longrightarrow 0$ of vanishing lattice spacing. In this limit, the quantity $\tilde{m}_l$ accurately corresponds to the light-quark mass describing the long-distance physics determined by our lattice theory. Likewise, the arguments given in Appendix A imply that in this limit, the spectral density $\rho(\Lambda)$ also approaches a continuum limit which requires $\Lambda \geq \tilde{m}_l$.

However, in the calculation presented here the lattice spacing a is relatively large and deviations from the inequality $\Lambda \geq \tilde{m}_l$ should be expected. In order to present the more conventional eigenvalue distribution $\rho(\lambda)$ while at the same time displaying the imperfections arising from finite a, we choose to plot the eigenvalue histograms in a hybrid form. For each of the original eigenvalues Λ we compute the derived eigenvalue $\lambda_n = \sqrt{\Lambda^2 - \tilde{m}_l^2}$. If λ_n is real, it is included in the histogram in the normal way, along the positive x axis. However, if λ_n is imaginary it is displayed in the same histogram along the negative x axis in a bin corresponding to $-|\lambda|$.

This has been done in the right-hand panel of Fig. 4. The histogram for $\lambda > 0$ is the conventional eigenvalue distribution, normalized in the $\mu = 2$ GeV, $\overline{\text{MS}}$ scheme. The histogram bins for $\lambda < 0$ are unphysical and directly result from finite lattice spacing artifacts. By showing both on the same plot, we make it easy to recognize the magnitude of the errors inherent in $\rho(\lambda)$, $\lambda > 0$ introduced by lattice artifacts. For example, it is likely that a majority of the gap in $\rho(\lambda)$ for λ positive but near zero in the right-hand panel of Fig. 4 would be filled in as $a \longrightarrow 0$ by the imaginary values of λ plotted as $-|\lambda| < 0$, and should not be attributed to the effects of finite volume.

An interesting test of these methods can be made by comparing the spectrum shown in the right-hand panel of Fig. 4 with the predictions of the Banks-Casher formula which relates the eigenvalue density $\rho(\lambda)$ at $\lambda = 0$ and the chiral condensate $\langle \bar{\psi}\psi \rangle$ when both are evaluated in the limit of infinite volume and vanishing quark mass,

$$\langle \bar{\psi}\psi \rangle = \pi\rho(0). \tag{23}$$

The right- and left-hand sides of Eq. (23) can be compared by examining the right-hand panel of Fig. 4 where we have superimposed the quantity $\langle \bar{\psi}\psi \rangle/\pi$ as horizontal lines on the histogram. Two values for $\langle \bar{\psi}\psi \rangle/\pi$ are shown. The upper line corresponds to $\langle \bar{\psi}_l \psi_l \rangle/\pi$ with finite light-quark mass $m_l = 0.003$. The lower horizontal line corresponds to the quantity $\Delta_{l,s}/\pi$ given by

$$\Delta_{l,s} = \langle \bar{\psi}_l \psi_l \rangle - \frac{m_l}{m_s} \langle \bar{\psi}_s \psi_s \rangle. \tag{24}$$

The subtraction is an attempt to remove a portion of the large, ultraviolet divergent contribution to $\langle\bar{\psi}\psi\rangle$, of the form m/a^2, expected for nonzero mass and finite L_s. This subtracted quantity is a more realistic estimate of $\langle\bar{\psi}\psi\rangle/\pi$ in the massless limit. To test the Banks-Casher relation, we compare the value of $\Delta_{l,s}/\pi$ with $\rho(\lambda)$ for small λ, as can be seen in the right panel of Fig. 4. This shows a value for $\Delta_{l,s}/\pi$ about 30% lower than $\rho(0)$, probably indicating that our 16^3 lattice results are significantly distorted by finite volume effects.

However, for the case of domain wall fermions there will be a residual mixing between the two fermion chiralities on the left and right walls when their separation L_s is finite. For long-distance quantities, this just results in an additive renormalization of the quark masses by $m_{\rm res}$. However, as suggested by the results in [28], the effects of residual chiral symmetry breaking on the dimension three operator $\bar{\psi}\psi$ may come from higher energies and be more perturbative than those contributing to $m_{\rm res}$, and therefore may fall off exponentially with L_s rather than as a power law. If that is also the case for the present ensembles with $L_s \geq 32$, the residual contribution to $\langle\bar{\psi}\psi\rangle$ is not very large and the subtraction in Eq. (24) may remove the dominant contributions to $\langle\bar{\psi}\psi\rangle$ from short-distance modes. However, the use of the DSDR action enhances the contribution of the exponential- relative to the power-suppressed residual chiral symmetry breaking, so neglecting $m_{\rm res}$ in Eq. (24) may not be as accurate on the DSDR ensembles as it would be on DWF ensembles where DSDR is not employed.

IV. OBSERVABLES PROBING THE CHIRAL SYMMETRIES OF QCD

In this section we introduce some observables used in our finite temperature calculations and discuss their connections to the $SU(2)_L \times SU(2)_R$ symmetry and the anomalous $U(1)_A$ symmetry of QCD.

The most basic observable indicating chiral symmetry restoration is the chiral condensate. In the chirally symmetric phase this quantity should vanish in the chiral limit. The single-flavor light and strange quark chiral condensates are defined as

$$\langle\bar{\psi}_q\psi_q\rangle = \frac{T}{V}\frac{\partial \ln Z}{\partial m_q} = \frac{1}{N_\sigma^3 N_\tau}\langle {\rm Tr} M_q^{-1}\rangle, \qquad q = l, s, \tag{25}$$

where M_q is the single-flavor Dirac matrix.[1] As discussed in the previous section, the leading ultraviolet divergent part in the chiral condensate is of the form $\sim m_q/a^2$. Thus, in order to eliminate this ultraviolet divergent contribution we construct the subtracted chiral condensate, $\Delta_{l,s}$, as defined in Eq. (24).

Chiral symmetry restoration can also be probed by studying various two-point functions. For computational simplicity, we will focus on various integrated two-point functions, i.e., susceptibilities, instead of the two-point correlations functions themselves.

The flavor nonsinglet (δ) and the flavor singlet (σ) two-point scalar correlators are given by

$$G_\delta(x) = -{\rm tr}\langle M_l^{-1}(x,0) M_l^{-1}(0,x)\rangle \tag{26}$$

and

$$G_\sigma(x) = G_\delta(x) + \langle {\rm tr} M_l^{-1}(x,x) {\rm tr} M_l^{-1}(0,0)\rangle - \langle {\rm tr} M_l^{-1}(x,x)\rangle\langle {\rm tr} M_l^{-1}(0,0)\rangle, \tag{27}$$

where the vacuum contribution to the σ correlator has been explicitly subtracted. By integrating these quantities over the four-volume one obtains the corresponding susceptibilities

$$\chi_\delta = \sum_x G_\delta(x) = \chi_{\rm con} \tag{28}$$

and

$$\chi_\sigma = \sum_x G_\sigma(x) = \chi_{\rm con} + \chi_{\rm disc}, \tag{29}$$

where the quark-line disconnected and the quark-line connected parts of the chiral susceptibilities[2] can be written, respectively, by

$$\chi_{\rm disc} = \frac{1}{N_\sigma^3 N_\tau}\{\langle({\rm Tr} M_l^{-1})^2\rangle - \langle {\rm Tr} M_l^{-1}\rangle^2\} \tag{30}$$

and

$$\chi_{\rm con} = -{\rm tr}\sum_x \langle M_l^{-1}(x,0) M_l^{-1}(0,x)\rangle \equiv -\frac{1}{N_\sigma^3 N_\tau}\langle {\rm Tr} M_l^{-2}\rangle. \tag{31}$$

The notation "tr" indicates traces over spinor and color indices only, while "Tr" also includes a trace over the discrete points $x = (x_0, \vec{x})$ in the four-volume. Tables IX and X summarize our results for the chiral condensates and disconnected chiral susceptibility, for the $L_s = 96$ and the DSDR ensembles, respectively. For both ensembles, the chiral condensates were obtained from a stochastic approximation in which the trace in Eq. (25) is estimated by the average over the diagonal matrix elements of M_l^{-1} evaluated on ten Gaussian random sources at every fifth molecular dynamics time unit. To compute the disconnected susceptibility, the term $\langle({\rm Tr} M_l^{-1})^2\rangle$ in Eq. (30) is calculated by averaging on each configuration only the

[1] For simplicity, we assign the quantity $\langle\bar{\psi}\psi\rangle$ a positive sign corresponding to using the mass term $-m\bar{\psi}\psi$ in the Dirac Hamiltonian.

[2] These quantities are referred to as chiral susceptibilities since they are related to the fluctuations of the quantity whose expectation value is the chiral condensate.

TABLE IX. Chiral condensates and the disconnected light-quark chiral susceptibility for the $L_s = 96$ ensembles.

T (MeV)	β	$\langle\bar{\psi}_l\psi_l\rangle/T^3$	$\langle\bar{\psi}_s\psi_s\rangle/T^3$	$\chi_{\rm disc}/T^2$
137	1.965	15.1(2)	37.6(1)	20(2)
146	1.9875	13.2(1)	35.99(7)	26(4)
151	2.00	12.0(2)	35.26 (9)	24(4)
156	2.0125	10.3(2)	33.92(12)	30(5)
162	2.025	10.1(2)	33.44(10)	24(4)
167	2.0375	8.0(2)	31.99(10)	29(3)
173	2.05	7.4(2)	31.48(10)	20(3)
188	2.08	6.2(2)	29.84(10)	21(3)
198	2.10	5.2(2)	28.68(10)	16(3)

product of matrix elements coming from different random sources. This ensures that the noise introduced by the Gaussian random vectors does not bias our estimate of $\chi_{\rm disc}$. (This strategy was also employed in computing the disconnected susceptibility, $\chi_{5,\rm disc}$, given later in Table XII.)

Chiral symmetry restoration implies a massless σ meson at the transition temperature. However, the δ meson is expected to remain massive unless the $U(1)_A$ symmetry also becomes restored at that temperature. Thus, at the chiral transition χ_σ will diverge, while χ_δ remains finite. This implies [see Eqs. (29) and (28)] that the disconnected part of the chiral susceptibility $\chi_{\rm disc}$ diverges at the chiral transition while the connected part $\chi_{\rm con}$ remains finite. At the chiral transition the diverging disconnected chiral susceptibility is expected to be related to the $O(4)$ scaling properties of the chiral transition. This in turn suggests that for nonzero light-quark mass (or finite volume) the chiral crossover temperature can be naturally identified by locating the maximum of the disconnected chiral susceptibility as a function of the temperature.

We also introduce flavor nonsinglet (π) and singlet (η) pseudoscalar two-point screening correlation functions,

$$G_\pi(x) = \mathrm{tr}\langle\gamma_5 M_l^{-1}(x,0)\gamma_5 M_l^{-1}(0,x)\rangle \tag{32}$$

and

$$G_\eta(x) = G_\pi(x) - \langle\mathrm{tr}[\gamma_5 M_l^{-1}(x,x)]\mathrm{tr}[\gamma_5 M_l^{-1}(0,0)]\rangle. \tag{33}$$

Integrating these correlation functions over the four-volume we obtain the corresponding pseudoscalar susceptibilities

$$\chi_\pi = \sum_x G_\pi(x) \equiv \chi_{5,\rm con} \tag{34}$$

and

$$\chi_\eta = \sum_x G_\eta(x) \equiv \chi_{5,\rm con} - \chi_{5,\rm disc}. \tag{35}$$

Table XI summarizes the details of our screening correlator measurements on the DSDR ensembles.

The scalar and pseudoscalar correlation functions introduced above are related through $SU(2)_L \times SU(2)_R$ flavor transformations, as illustrated by the horizontal lines in Fig. 5. Hence, utilizing Eqs. (29), (28), (34), and (35), chiral symmetry restoration is manifested through the following degeneracies among the susceptibilities of the two-point correlation functions:

$$\chi_\pi = \chi_\sigma \Rightarrow \chi_\pi - \chi_\delta = \chi_{\rm disc} \tag{36}$$

and

$$\chi_\delta = \chi_\eta \Rightarrow \chi_\pi - \chi_\delta = \chi_{5,\rm disc}. \tag{37}$$

In the limit of two massless flavors, the anomalous $U(1)_A$ symmetry cannot be probed with a local expectation value such as the chiral condensate. In this case it is necessary to use two-point correlation functions, as introduced above [53–55]. Since the $U(1)_A$ transformation does not change the flavor quantum numbers, a restoration of $U(1)_A$ symmetry will be manifested by the equalities between the following susceptibilities:

$$\chi_\pi = \chi_\delta \quad \text{and} \quad \chi_\sigma = \chi_\eta. \tag{38}$$

Thus, the susceptibility difference $\chi_\pi - \chi_\delta$ can be used to study restoration of $U(1)_A$ symmetry at high temperatures. Note, while both the susceptibilities χ_π and χ_δ individually contain an additive ultraviolet divergent term $\sim 1/a^2$, their difference is free of this divergence. Furthermore, in the chirally symmetric phase of QCD one can use Eqs. (36) and (37) to obtain

TABLE X. Chiral condensates and the disconnected light-quark chiral susceptibility for the DSDR ensembles.

Label	T (MeV)	$\langle\bar{\psi}\psi\rangle_l/T^3$	$\langle\bar{\psi}\psi\rangle_s/T^3$	$\Delta_{l,s}/T^3$	$\chi^{\rm bare}_{\rm disc}/T^2$	$\chi^{\overline{\rm MS}}_{\rm disc}/T^2$
1	139	9.23(14)	41.00(5)	10.30(14)	37(3)	17.2(1.4)
2	149	6.26(12)	36.42(5)	7.74(12)	44(3)	19.9(1.0)
3	149	8.39(10)	38.30(3)	7.06(10)	41(2)	18.5(0.9)
4	159	5.25(17)	33.81(6)	4.83(17)	43(4)	18.8(1.8)
5	168	4.03(18)	30.66(7)	2.78(18)	35(5)	14.9(2.1)
6	177	3.16(15)	27.88(6)	1.56(15)	25(4)	10.4(1.7)
7	186	2.44(9)	25.43(4)	0.71(9)	11(4)	4.5(1.6)
8	195	2.07(9)	23.24(5)	0.34(9)	5(3)	2.0(1.2)

TABLE XI. Summary of screening correlator measurements. All measurements are with a point source and point sink with the source located at $(x, y, z, t) = (0, 0, 0, 0)$.

Label	T (MeV)	Trajectories	Step
1	139	200–2990	10
3	149	300–7000	5
4	159	300–3650	10
5	168	300–3410	10
6	177	300–1780	10
7	186	300–4360	10
8	195	302–2447	5
		2450–6000	5

$$\chi_\pi - \chi_\delta = \chi_{\rm disc} = \chi_{5,\rm disc}, \qquad \text{for } T \geq T_c,\ m_l \to 0. \tag{39}$$

Hence, in the chirally symmetric phase (in the chiral limit) the disconnected chiral susceptibility itself can be used to probe the restoration of the $U(1)_A$ symmetry.

This conclusion exemplifies the importance of the disconnected chiral susceptibility as a probe of the character of the QCD phase transition. If $U(1)_A$ symmetry is broken above T_c and the transition belongs to the $O(4)$ universality class, then we expect singular behavior for $\chi_{\rm disc}$ as $T \to T_c^+$:

$$\chi_{\rm disc} \sim (T - T_c)^{-\gamma} \tag{40}$$

for $m_q = 0$ and $T > T_c$ where $\gamma = 1.453$ [56]. If instead $U(1)_A$ symmetry is essentially restored above T_c, i.e. all anomaly-related breaking effects can be neglected, then $\chi_{\rm disc}$ must vanish for $T > T_c$ while for $T < T_c$ it must diverge as $m_q \to 0$ because of the existence of massless pions. Thus, $\chi_{\rm disc}$ must again show singular behavior at T_c.

Further information about $\chi_\pi - \chi_\delta$ can be obtained by comparing to the topological charge, $Q_{\rm top}$. $Q_{\rm top}$ is defined as

$$Q_{\rm top} = \frac{g^2}{32\pi^2} \int d^4x F^a_{\mu\nu}(x) \tilde{F}^a_{\mu\nu}(x). \tag{41}$$

On a smooth gauge configuration, if lattice artifacts are small, the topological charge and the integrated pseudoscalar bilinear can be related:

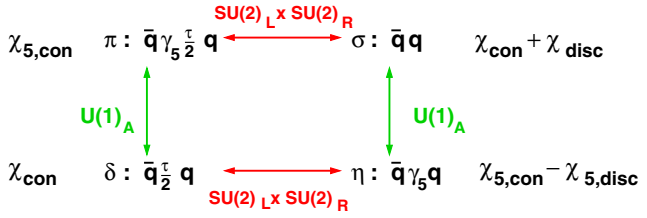

FIG. 5 (color online). Symmetry transformations relating scalar and pseudoscalar mesons in flavor singlet and nonsinglet channels.

$$Q_{\rm top} = m_l \int d^4x \bar{\psi}_l(x) \gamma_5 \psi_l(x). \tag{42}$$

If this relation is squared, averaged over the gauge field and divided by the space-time volume V, we obtain a relation between the topological susceptibility and the disconnected pseudoscalar susceptibility:

$$\chi_{\rm top} = \frac{\langle Q^2_{\rm top} \rangle}{V} = m_l^2 \chi_{5,\rm disc}. \tag{43}$$

This equation can be obtained in the continuum theory by integrating the anomalous conservation law for the axial current over space-time, squaring the result, dividing by the space-time volume and ignoring possible ambiguities in the operator product appearing in $Q^2_{\rm top}$. If we assume $SU(2)_L \times SU(2)_R$ symmetry and substitute Eq. (39) into Eq. (43), we can directly relate the measure of $U(1)_A$ symmetry breaking $\chi_\pi - \chi_\delta$ and the topological susceptibility:

$$\chi_\pi - \chi_\delta = \frac{1}{m_l^2} \chi_{\rm top}. \tag{44}$$

Finally, the eigenvalue spectrum of the Dirac operator is also intimately connected with the chiral and anomalous axial symmetry. The symmetry-breaking quantities $\langle \bar{\psi}\psi \rangle$ and $\chi_\pi - \chi_\delta$ can both be expressed in terms of the eigenvalue spectrum of the Dirac operator in the following way:

$$\langle \bar{\psi}_l \psi_l \rangle = \int_0^\infty {\rm d}\lambda \frac{2 m_l \rho(\lambda)}{m_l^2 + \lambda^2}, \tag{45}$$

$$\chi_\pi - \chi_\delta = \int_0^\infty {\rm d}\lambda \frac{4 m_l^2 \rho(\lambda)}{(m_l^2 + \lambda^2)^2}. \tag{46}$$

Equation (45) is the basis of the Banks-Casher relation [57] which connects the chiral condensate to the density of zero eigenvalues $\lim_{m_l \to 0} \langle \bar{\psi}_l \psi_l \rangle = \pi \rho(0)$. While in the chirally broken phase a nonzero value of the chiral condensate demands $\rho(0) \neq 0$, in the chirally symmetric phase a vanishing chiral condensate leads to $\rho(0) = 0$. However, Eq. (46) shows that a nonzero anomalous symmetry-breaking difference $\chi_\pi - \chi_\delta$ in the limit of massless quarks requires complex behavior for $\rho(\lambda)$ as λ approaches zero [58]. This required behavior is very different, for example, from that found in the case of a free field at finite temperature. For the free field case there is a gap in the spectrum between zero and the Matsubara frequency πT: $\rho(\lambda) = 0$ for $0 \leq \lambda < \pi T$. This question is studied in detail in Sec. VI.

V. $SU(2)_L \times SU(2)_R$ RESTORATION

We now turn to a discussion of $SU(2)_L \times SU(2)_R$ chiral symmetry restoration. We will first discuss the chiral transition using conventional observables such as the chiral condensate and the related chiral susceptibility.

We then will turn to a discussion of several hadronic susceptibilities.

In Fig. 6 we show results for the light-quark chiral condensate calculated on the $16^3 \times 8$ ensembles in the temperature range 139 MeV $\leq T \leq$ 195 MeV. In this figure, we also show the subtracted chiral condensate $\Delta_{l,s}$ introduced in Eq. (24). The values plotted at the lower two temperatures, $T = 139$ and 149 MeV, were obtained using $L_s = 48$ while the values at the five higher temperatures use $L_s = 32$. As discussed in Sec. II, the ultraviolet divergent piece of the chiral condensate, m_l/a^2 is sensitive to the bare light-quark mass. This results in the irregular behavior for the light-quark chiral condensate seen in Fig. 6 and the different values for this quantity for ensembles #2 and #3 given in Table X. As also should be expected, this short-distance contribution to $\langle \bar{\psi}\psi \rangle$ is substantially reduced in the subtracted quantity $\Delta_{l,s}$, which agrees between $L_s = 32$ and 48 at $T = 149$ MeV at the 10% level.

As described in Sec. IV we can use the fluctuations found in our calculation of the expectation values of $\bar{\psi}\psi$ and $\bar{\psi}\gamma_5\psi$ to construct the disconnected part of the chiral susceptibility. The upper panel of Fig. 7 shows our results for the disconnected chiral susceptibility from both the $L_s = 96$ and the $L_s = 32$ and 48 results calculated with the DSDR gauge action. The discrepancy between the two results for $T \leq 170$ MeV can be explained by the different values of the light-quark mass used in the two calculations. The $L_s = 96$ calculation was performed with the quark mass fixed in lattice units and the resulting zero-temperature pion mass decreasing from approximately 275 to 225 MeV as the temperature decreases from the highest to the lowest value. In contrast, the DSDR calculation was performed at a fixed 200 MeV pion mass. Since the disconnected chiral susceptibility is expected to increase as the pion mass decreases for $T \leq T_c$, a larger value should be expected from the DSDR calculation in this temperature range. For temperatures above the transition, the chiral condensate and to some degree its fluctuations are suppressed by a decreasing physical quark mass, causing the DSDR values for $\chi_{\rm disc}$ to fall below those of the $L_s = 96$ ensemble.

In the lower panel of Fig. 7 we compare the DSDR, DWF results with those obtained previously using the asqtad and HISQ staggered fermions by the HotQCD collaboration [59]. In order to make a comparison between different fermion actions, one must convert the unrenormalized results for the disconnected chiral susceptibility into a common renormalization scheme, e.g. the $\overline{\rm MS}$ scheme that was discussed in Sec. III. The renormalized chiral susceptibility is given by

$$\chi_{\rm disc}^{\overline{\rm MS}} = \left(\frac{1}{Z_{m_f \to \overline{\rm MS}}(\mu^2)}\right)^2 \chi_{\rm disc}^{\rm bare}, \tag{47}$$

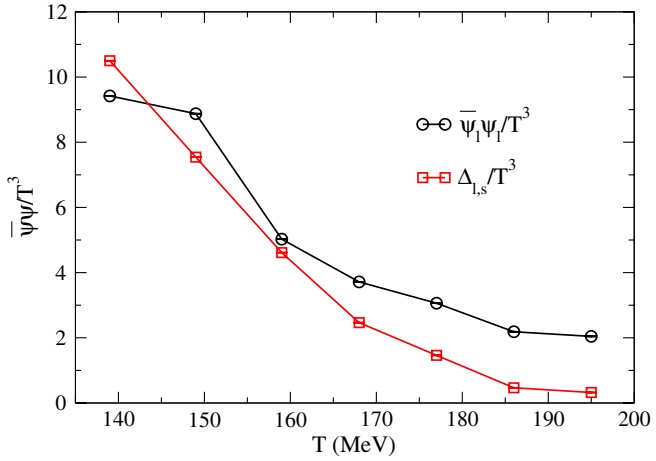

FIG. 6 (color online). The light-quark chiral condensate, as well as the subtracted chiral condensate plotted as a function of temperature. As discussed in the text, the values plotted for $T = 139$ and 149 MeV were computed using $L_s = 48$ while those at higher temperatures used $L_s = 32$.

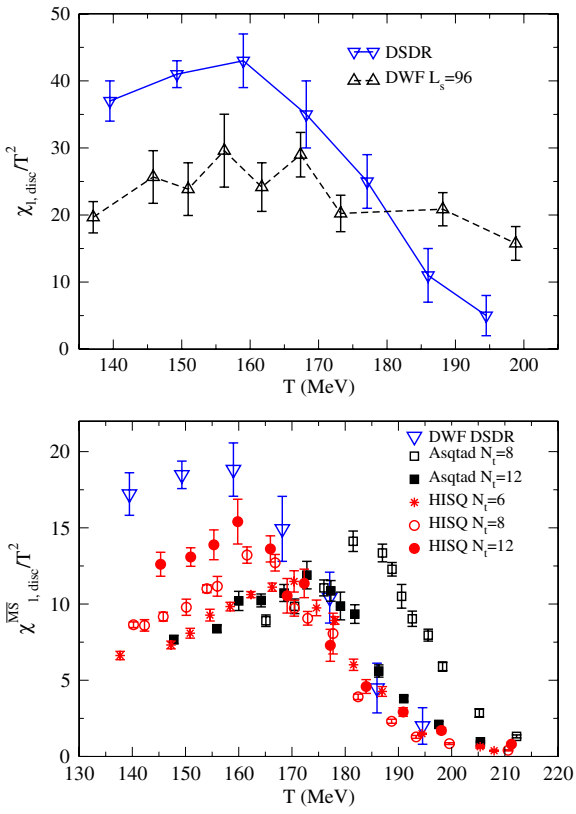

FIG. 7 (color online). In the upper panel, the unrenormalized, disconnected chiral susceptibility for DWF DSDR $L_s = 32, 48$ is compared with the DWF results with $L_s = 96$. In the lower panel, the renormalized chiral susceptibilities, converted to the $\overline{\rm MS}$ scheme are compared between the DWF DSDR calculation and the HISQ and asqtad results from the HotQCD Collaboration, corresponding to a pseudo-Goldstone pion mass of 161 and 179 MeV, respectively.

where an expression for $Z_{m_f\to\overline{\rm MS}}(\mu^2)$ is given in Eq. (18). The values of $Z_{m_f\to\overline{\rm MS}}(\mu^2)$ are tabulated for the DWF + DSDR action with $\mu = 2$ GeV in Table VII. Details for converting the staggered results to the $\overline{\rm MS}$ scheme are discussed in Appendix B.

The difference between the DWF and staggered results shown in the lower panel of Fig. 7 may arise from more than one source. While the staggered results are obtained with nominally lighter pion masses (the $N_t = 12$ HISQ and asqtad results have $m_\pi = 161$ and 179 MeV, respectively), this is the mass of the lightest Goldstone pion and taste breaking leads to a range of masses for the other 15 taste-split pions, some of which are considerably larger. In contrast, the DWF calculation has three degenerate 200 MeV pions. However, the staggered calculations are performed at much larger physical volumes than the DWF work reported here, with linear dimensions twice the size of those in the DWF calculation. In fact, a finite volume scaling study of an $O(4)$ symmetric quark-meson model of the phase transition [60] suggests that the height of the peak in the chiral susceptibility associated with the transition should become smaller as the volume is increased, which provides a second possible explanation of the discrepancy between the DWF and staggered results found in Fig. 7.

To obtain the connected part of the various susceptibilities we have calculated hadronic correlation functions in different quantum number channels (for a more detailed discussion see Sec. IV). The sink position of these two-point correlation functions is then integrated over the full space-time volume to obtain the corresponding susceptibility. For example, the integral over the scalar point-point correlation function gives the connected part of the chiral susceptibility $\chi_{l,\rm con} \equiv \chi_\delta$, with χ_δ introduced in Eq. (28).

We find that susceptibilities calculated from connected correlation functions do not show significant temperature dependence. This is quite similar to what has been found in calculations performed with staggered fermions. While dramatic temperature dependence is expected in the connected susceptibilities, for example, in χ_π associated with the small pion mass below T_c, these quantities are likely dominated by the $1/a^2$ divergence associated with the coincidence of the source and sink points when the correlation function is integrated over space-time.

In the chiral limit the restoration of chiral flavor symmetry can also be seen in the vanishing of the susceptibilities differences $\chi_\pi - \chi_\sigma$ and $\chi_{\rm disc} - \chi_{5,\rm disc}$ as shown in Eq. (39). We show these two measures of chiral symmetry breaking in Fig. 8 where one sees a decrease with increasing temperature that is even more rapid than that found in Fig. 6 for the subtracted chiral order parameter $\Delta_{l,s}$.

The two differences $\chi_\pi - \chi_\sigma$ and $\chi_{\rm disc} - \chi_{5,\rm disc}$ provide information on chiral symmetry restoration that is consistent with the observed peak in the disconnected chiral susceptibility. All three observables suggest that the transition to the chirally symmetric, high-temperature phase occurs at a temperature of about $T \sim$ (160–170) MeV. We should stress, however, that this result has been obtained at a single value of the lattice cutoff and from simulations performed in a rather small physical volume, $N_L/N_T = V^{1/3}T = 2$. In an $O(4)$ scaling study of a model of the transition, Braun *et al.* [60] find that the pseudocritical transition temperature shifts to larger values when the volume is increased. As mentioned above, these finite volume effects also are expected to account for the larger height of the susceptibility peak found when comparing our DWF calculations to the larger-volume staggered results.

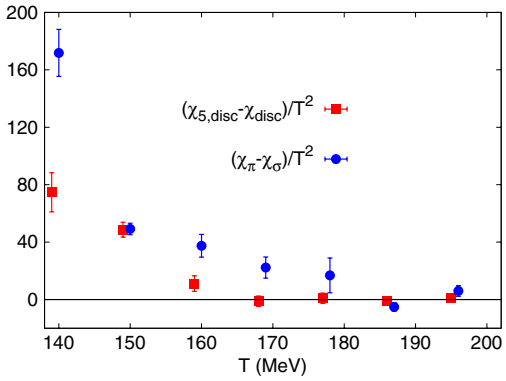

FIG. 8 (color online). The $SU(2)_L \times SU(2)_R$-breaking differences between the disconnected pseudoscalar and disconnected scalar susceptibilities and between the flavor-triplet pseudoscalar and flavor singlet scalar susceptibilities.

VI. ANOMALOUS $U(1)_A$ BREAKING ABOVE T_c

In this section we examine the strength of anomalous axial symmetry breaking as a function of temperature and attempt to determine its origin. For temperatures below T_c the nonvanishing light-quark chiral condensate, $\langle\bar\psi_l\psi_l\rangle$ which breaks the nonanomalous $SU(2)_L \times SU(2)_R$ chiral symmetry also breaks the anomalous symmetry. This large vacuum $U(1)_A$ asymmetry obscures other possible sources of anomalous symmetry breaking so that the effects of the axial anomaly are rather subtle, appearing, for example, in the splitting between the mass of the SU(3) flavor singlet η' meson and the SU(3) flavor octet of pseudo-Goldstone bosons. However, as the temperature is increased above T_c this vacuum symmetry breaking disappears (as discussed in Sec. V) so that the remaining $U(1)_A$ symmetry breaking must come from the axial anomaly present in the underlying quantum field theory.

At high temperatures the anomalous symmetry breaking can be described using a semiclassical expansion known as the dilute instanton gas approximation (DIGA). In the DIGA, the Euclidean finite temperature path integral is described as an integral over quantum fluctuations about a series of classical Yang-Mills background fields constructed from a superposition of widely separated

instanton and anti-instanton classical solutions. Here the (anti)instanton size will be on the order of or smaller than $1/T$ and the one-loop quantum corrections imply an instanton-anti-instanton density $\propto m_l^{N_f} \exp\{-8\pi^2/g(T)^2\}$ [61]. The integer N_f is the number of light flavors, which have a small common mass m_l, and $g(T)$ is the running Yang-Mills coupling constant evaluated at the momentum scale $\mu \sim T$. The nonzero topological charge density, $(g^2/32\pi^2)F^{\mu\nu}(x)\tilde{F}^{\mu\nu}(x)$ in the DIGA can be directly related to the anomalous breaking of $U(1)_A$ symmetry through the familiar anomaly equation:

$$\partial_\mu \sum_{i=1}^{N_f} \bar{\psi}_i \gamma^5 \gamma^\mu \psi_i = 2m_l \sum_{i=1}^{N_f} \bar{\psi}_i \gamma^5 \psi_i + N_f \frac{g^2}{16\pi^2} F^{\mu\nu}\tilde{F}^{\mu\nu}. \tag{48}$$

The detailed mechanism of anomalous symmetry breaking which realizes the consequences of Eq. (48) is well understood as the effects of infrared singularities associated with the N_f fermion near-zero modes that are located at each of the instantons and anti-instantons in this semiclassical description. For example, in Eq. (46) the $U(1)_A$-asymmetric difference between the isovector pseudoscalar and scalar susceptibilities, $\chi_\pi - \chi_\delta$ is expressed in terms of an integral over the Dirac eigenvalue density $\rho(\lambda)$, divided by an infrared-singular denominator vanishing as m_l and λ approach zero. The DIGA in the case of N_f degenerate light flavors implies the existence of Dirac near-zero modes whose contribution to the eigenvalue spectrum should be well approximated by

$$\rho(\lambda) \approx c(T) m^{N_f} \delta(\lambda). \tag{49}$$

The use of the delta function $\delta(\lambda)$ neglects the small splitting from zero for these near-zero modes which results from the interactions between the widely separated instantons and anti-instantons in the "dilute" gas. Although Eq. (46) contains two powers of the fermion mass and naively vanishes in the chiral limit, this infrared divergent denominator $(\lambda^2 + m^2)^2$, when combined with the eigenvalue density in Eq. (49), implies a nonzero value for $\chi_\pi - \chi_\delta = 2c(T)$ for the case of two light flavors in the limit of vanishing quark mass.

While the DIGA is expected to be the correct description of QCD thermodynamics at high temperature, one might imagine a more complex mechanism for anomalous symmetry breaking when the temperature is lower and this semiclassical, perturbative treatment of widely separated instantons and anti-instantons is invalid. For example, at lower temperatures still above T_c one might imagine a nonperturbative accumulation of small eigenvalues which leads to a density $\rho(\lambda, m) = m^{\nu_m}\lambda^{\nu_\lambda}$. For $T > T_c$ the vanishing of the chiral condensate and the Banks-Casher relation requires $\nu_m + \nu_\lambda > 0$. However, examining Eq. (46) we see that the $U(1)_A$-breaking difference $\chi_\pi - \chi_\delta$ will remain finite in the limit of vanishing quark mass for the present case of two light flavors if $\nu_m + \nu_\lambda \leq 1$. Similar possible $U(1)_A$-symmetry-breaking behaviors have been discussed previously [23,58,62].

We will now examine our numerical results for anomalous symmetry breaking and their correlation with gauge-field topology as well as the Dirac eigenvalue spectrum itself. In particular, we will discuss the anomalous symmetry-breaking differences in both connected and disconnected susceptibilities as well as in the underlying Green's functions evaluated in position space. We will also compare our results with the predictions of the high-temperature DIGA and search for possible new mechanisms for $U(1)_A$ symmetry breaking at temperatures closer to T_c.

A. Connected and disconnected susceptibilities

As discussed in Sec. IV, an accessible observable to examine is the $U(1)_A$ symmetry-breaking difference $\chi_\pi - \chi_\delta$. In that section we also showed in Eq. (39) that the difference $\chi_\pi - \chi_\delta$, the disconnected chiral susceptibility $\chi_{\rm disc}$, and the disconnected pseudoscalar susceptibility $\chi_{5,\rm disc}$ all become equal in the chiral limit for $T \geq T_c$ as a direct consequence of $SU(2)_L \times SU(2)_R$ symmetry. In addition, $\chi_\pi - \chi_\delta$ is directly related to the Dirac eigenvalue density through Eq. (46).

These three observables are plotted in Fig. 9 and their numerical values for the DSDR ensembles are given in Tables X and XII. All three, $\chi_{\rm disc}$, $\chi_{5,\rm disc}$ and $\chi_\pi - \chi_\delta$, agree within errors for $T \geq 168$ MeV suggesting both a restoration of vacuum $SU(2)_L \times SU(2)_R$ symmetry and

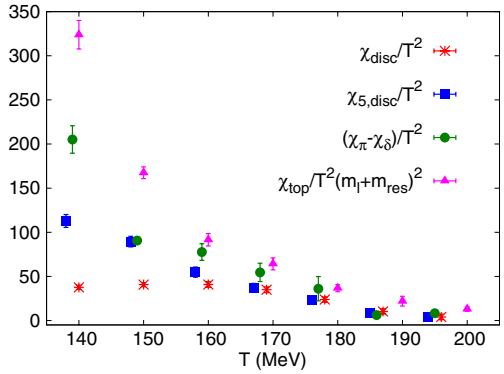

FIG. 9 (color online). The disconnected scalar (chiral) and pseudoscalar susceptibilities plotted versus temperature as crosses and squares, respectively. The circles show the $U(1)_A$-breaking difference $\chi_\pi - \chi_\delta$, which in the chiral limit will become equal to both disconnected susceptibilities above T_c. Finally, the triangles represent the topological susceptibility divided by the square of the total bare quark mass, $m_f + m_{\rm res}$, a combination which should equal the pseudoscalar susceptibility at all temperatures, as in Eq. (43). The large discrepancy between $\chi_{\rm top}/(m_f + m_{\rm res})^2$ and $\chi_{5,\rm disc}$ is believed to arise from large lattice artifacts in the determination of $\chi_{\rm top}$ as discussed below and in Appendix D.

TABLE XII. Our results for the susceptibilities χ_π, χ_δ, $\chi_\pi - \chi_\delta$, $\chi_{5,\mathrm{disc}}$, and χ_{top}.

Label	T (MeV)	χ_π/T^2	χ_δ/T^2	$(\chi_\pi - \chi_\delta)/T^2$	$\chi_{5,\mathrm{disc}}/T^2$	χ_{top}/T^2
1	139	283(11)	78(6)	205(16)	113(7)	$6.6(3) \times 10^{-3}$
2	149	178(3)	87(1)	91(4)	89(6)	$3.7(1) \times 10^{-3}$
4	159	177(7)	99(6)	78(9)	55(6)	$1.7(1) \times 10^{-3}$
5	168	139(7)	85(6)	55(10)	37(5)	$0.95(10) \times 10^{-3}$
6	177	113(9)	77(6)	36(14)	24(4)	$0.49(5) \times 10^{-3}$
7	186	93(2)	87(1)	6(2)	9(3)	$0.24(6) \times 10^{-3}$
8	195	88(2)	79(2)	8(4)	5(4)	$0.13(3) \times 10^{-3}$

that our $\sim$10 MeV quark mass and resulting 200 MeV pion introduce a sufficiently small explicit chiral symmetry breaking that its effects are not visible at our level of accuracy. Especially interesting is the fact that the $U(1)_A$ breaking difference, $\chi_\pi - \chi_\delta$, is nonzero throughout the temperature range considered here. This suggests that $U(1)_A$ remains explicitly broken even after chiral symmetry is restored. Furthermore, since the symmetry-breaking effects of the nonzero quark mass produce no visible discrepancies between χ_{disc}, $\chi_{5,\mathrm{disc}}$ and $\chi_\pi - \chi_\delta$, it is reasonable to expect that the difference between χ_π and χ_δ arises from the axial anomaly—not the nonzero quark mass.

Also shown in Fig. 9 is the combination $\chi_{\mathrm{top}}/(m_f + m_{\mathrm{res}})^2$ which is expected to be equal to the pseudoscalar susceptibility $\chi_{5,\mathrm{disc}}$, following Eq. (43). As can be seen in the figure this expectation is badly violated, with these two quantities differing by more than a factor of 2 at the lowest temperature. As is discussed in greater detail in Appendix D, we have examined our results for these two quantities carefully and believe that our calculation of χ_{top} is not reliable at the large lattice spacings and nonzero temperatures being explored here. The quantity $\chi_{5,\mathrm{disc}}$ is determined directly from the Dirac propagator on the lattice and has a well-understood continuum limit. In contrast, the topological susceptibility is obtained from an empirically justified procedure of gauge link smearing steps followed by the evaluation of an improved combination of links chosen to approximate the topological charge density $F\tilde{F}$. As shown in Appendix D, these two quantities do not agree at nonzero temperature, despite the fact that there is good agreement at zero temperature, even at our coarsest lattice spacings.

B. Position-space correlators

Additional understanding of this $U(1)_A$ symmetry violation comes from examining the spatial correlators themselves. We begin by writing the isovector scalar and pseudoscalar correlators (those for the δ and the π) in terms of their left- and right-handed components,

$$G_{\pi/\delta}(x) = \langle \bar{u}_L d_R(x) \bar{d}_R u_L(0) + \bar{u}_R d_L(x) \bar{d}_L u_R(0) \rangle \pm \langle \bar{u}_L d_R(x) \bar{d}_L u_R(0) + \bar{u}_R d_L(x) \bar{d}_R u_L(0) \rangle. \tag{50}$$

Here the left- and right-handed parts are defined as

$$u_{L/R}(x) = \left(\frac{1 \mp \gamma_5}{2}\right) u(x), \qquad d_{L/R}(x) = \left(\frac{1 \mp \gamma_5}{2}\right) d(x), \tag{51}$$

$$\bar{u}_{L/R}(x) = \bar{u}(x) \left(\frac{1 \pm \gamma_5}{2}\right), \qquad \bar{d}_{L/R}(x) = \bar{d}(x) \left(\frac{1 \pm \gamma_5}{2}\right). \tag{52}$$

In Eq. (50), the terms on the first line are invariant under $U(1)_A$ rotations. These occur with the same sign for both the δ and the π correlators. By contrast the terms on the second line, which occur with opposite signs for the two correlators, are not invariant under $U(1)_A$ transformations and their expectation value should therefore vanish in a $U(1)_A$-symmetric theory.

The invariant and noninvariant parts of these correlators may be isolated by taking the sum and difference, respectively, of the two correlators. These are shown in Fig. 10 for all the temperatures. Actually, what are plotted are the *screening correlators* $C(z)$, which are related to the corresponding point-to-point correlators by

$$C_H(z) = \sum_{x,y,\tau} G_H(x, y, z, \tau), \qquad H = \pi, \delta, \rho, \text{ etc.} \tag{53}$$

We see that the difference $C_\pi(z) - C_\delta(z)$ is always nonzero. For source-sink separations within a few lattice spacings of zero, this nonzero value is dwarfed by the much larger nonanomalous contribution to $C_\pi(z)$ and $C_\delta(z)$ and this disparity grows with increasing temperature. However, while its magnitude decreases as T is increased, the difference is always comparable to the sum $C_\pi(z) + C_\delta(z)$ at the largest source-sink separations viz. $x \approx N_\sigma/2$. This suggests a significant breaking of $U(1)_A$ symmetry for this long-distance quantity, even with increasing temperature. However, studies with a varying quark mass are required to establish this as an effect of the anomaly.

C. Correlation with topology

The connection between the $U(1)_A$-breaking difference $\chi_\pi - \chi_\delta$ and the topology of the gauge fields can be studied by comparing the Monte Carlo time histories for these two quantities. Figure 11 contains plots of the time

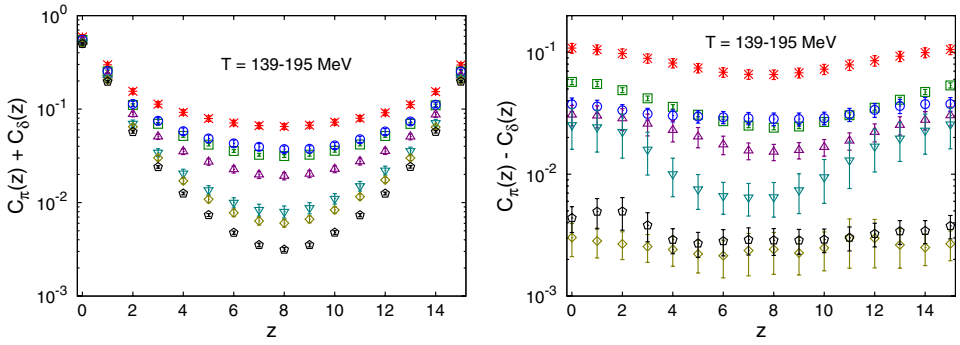

FIG. 10 (color online). (Left) The sum of the spatial π and the δ correlators. The temperature increases from $T = 139$ MeV to 195 MeV as one moves downward along the y axis. (Right) The difference $C_\pi(z) - C_\delta(z)$. The temperatures are identified by the same symbols as in the sum. The monotonic decreasing behavior seen with increasing temperature in the left panel is not seen for the highest temperatures in the right panel where the $T = 195$ MeV data lies slightly above that for $T = 186$. However, this apparent diminished rate of decrease with increasing temperature may be an artifact of insufficient statistics since the statistical errors on this signal, which, as discussed in Sec. VI C, arises from infrequent spikes in the data, may be underestimated.

histories of the measurements whose average gives the connected susceptibility difference $\chi_\pi - \chi_\delta$ and the topological charge Q_{top}. On our finite temperature gauge configurations, Q_{top} is computed on each gauge configuration using the five loop improved (5Li) gauge-field operator introduced in [31]. Q_{top} is measured after the gauge fields are smoothed by applying 60 APE smearing steps [63] with smearing coefficient $\epsilon = 0.45$, so that Q_{top} gives near-integer values. We see that $U(1)_A$ is not broken "on average" but rather only on specific configurations. These tend to be the configurations with $Q_{\text{top}} \neq 0$.

However, as discussed in Appendix D, the use of the 5Li method and cooled gauge fields to compute Q_{top} is contaminated by significant lattice artifacts, particularly at

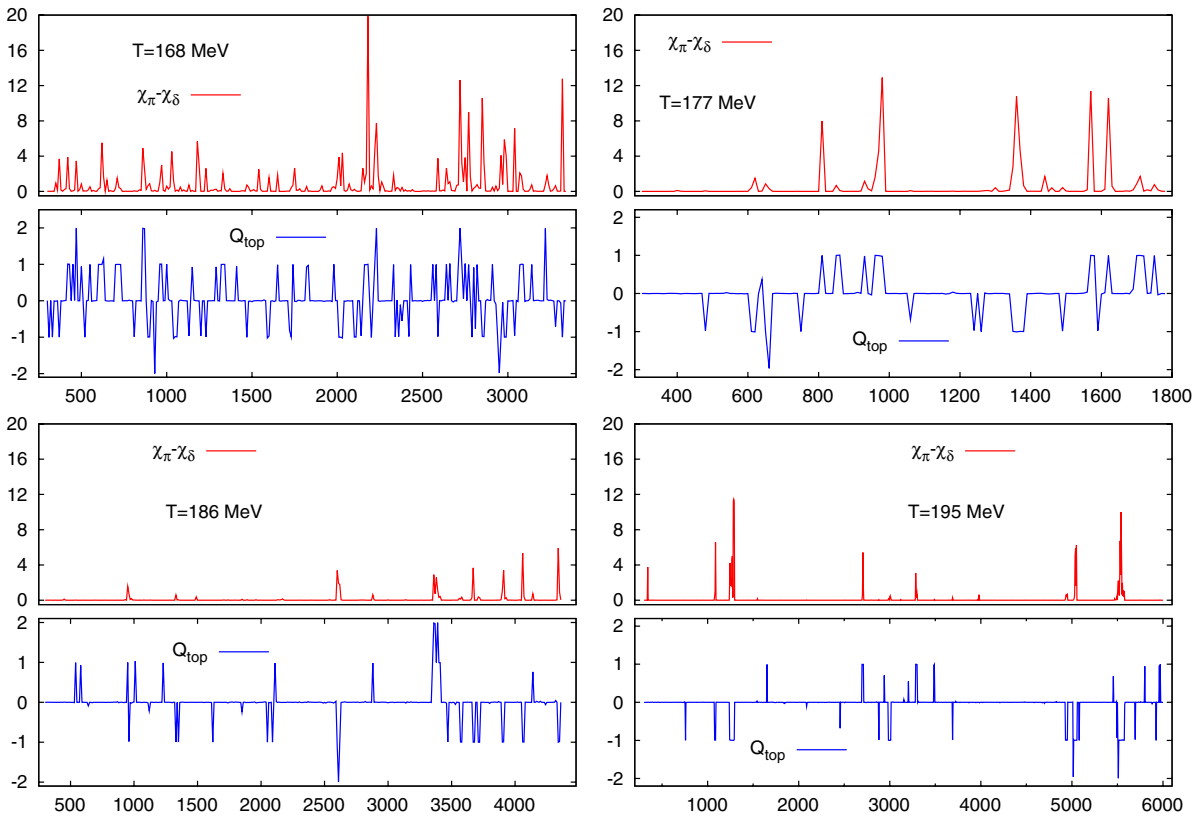

FIG. 11 (color online). The time histories for the topological charge (blue lines) and the integrated correlator $\chi_\pi - \chi_\delta$ (red lines) for $T = 168$–195 MeV. These time histories have been labeled with the quantities that result when those histories are time averaged.

stronger coupling. This is reflected by the less than perfect correlation between $Q_{\rm top}$ and contributions to $\chi_\pi - \chi_\delta$ in Fig. 11. On a few configurations with $Q_{\rm top}$ apparently nonzero there is no evident contribution to $\chi_\pi - \chi_\delta$ while on some other configurations with $Q_{\rm top} = 0$, there is a nonzero contribution to $\chi_\pi - \chi_\delta$.

Despite the imperfections in $Q_{\rm top}$, the correlation between $U(1)_A$ breaking and gauge-field topology can still be qualitatively observed in our data. This connection is similar to that predicted by the DIGA. However, in that picture $U(1)_A$ breaking is connected with the total number of instantons and anti-instantons, $N_I + N_{\bar{I}}$, not their difference, $N_I - N_{\bar{I}}$, which is determined by the gauge-field topology. For example, we should expect to occasionally see a configuration containing a widely separated instanton and anti-instanton in which the resulting two near-zero modes produce a large spike in the time history of $\chi_\pi - \chi_\delta$ but which does not appear in the time history of the topology. It is not obvious that there are examples of such a phenomena in Fig. 11. Of course, our volume may be too small for multiple instantons/anti-instantons. This is also suggested by the preponderance of three topological charges 0, ± 1 and reflected in the direct determination of the density of Dirac near-zero modes presented in the following section. Note, the fluctuations seen in the time histories of $\chi_\pi - \chi_\delta$ shown in Fig. 11 arise in part from the method used to calculate this quantity and have only an indirect physical meaning. At least a portion of these fluctuations arise from the occasional coincidence between the space-time location of the fixed point-source used in computing χ_π and χ_δ and the random location of a localized near-zero mode, rather than from an increased number of near-zero modes.

D. Dirac eigenvalue density

Since the infrared structure of QCD underlies the anomalous breaking of $U(1)_A$ symmetry, we expect that much can be learned from explicitly examining the eigenvalue spectrum of the Dirac operator near-zero eigenvalue. For earlier studies of the Dirac eigenvalue spectrum using staggered and overlap fermions see Refs. [26,64–68]. Knowing the Dirac spectrum, we can directly examine the eigenvalue density $\rho(\lambda)$, discussed in Sec. III, looking for the behavior as $\lambda \to 0$ necessary to produce a $U(1)_A$-breaking difference $\chi_\pi - \chi_\delta$ from Eq. (46). We can compare our calculated density of eigenvalues $\rho(\lambda)$ with what is expected in the case of a dilute instanton gas and look for possible new, $U(1)_A$-breaking behaviors as T approaches T_c from above. In this subsection we will first present our numerical results and then discuss possible behaviors for $\rho(\lambda, m)$ as the light-quark mass m_l and Dirac eigenvalue λ approach zero.

1. Numerical results for $\rho(\lambda)$

In Figs. 12–14 we present our results for the $\rho(\lambda)$, with both ρ and λ normalized in the $\mu = 2$ GeV, $\overline{\rm MS}$ scheme, determined from the 100 lowest eigenvalues calculated at each of six temperatures using the methods explained in Sec. III. The number of configurations used in each case varied from 239 to 1140 and is listed in Table VIII. Here we are presenting the lattice analogue of the usual Dirac eigenvalue λ from which the quark mass has been removed, $\lambda = \sqrt{\Lambda^2 - (m_f + m_{\rm res})^2}$. As explained in Sec. III, at finite lattice spacing this assumed mass dependence for the full Dirac eigenvalues Λ is only approximate and in some cases the argument of the square root is negative. In those cases the resulting λ is placed on the histogram at the unphysical position $-|\lambda|$, allowing this type of a^2 error to be recognized.

At both $T = 149$ and 159 MeV, the spectrum appears to be approaching a nonzero intercept as λ approaches zero until $\lambda \sim 10$ MeV, when the eigenvalue density decreases rapidly toward zero. As is suggested by the behavior of the chiral condensate in Fig. 6 and the disconnected chiral susceptibility in Fig. 7, both the 149 and 159 MeV temperatures lie close to the crossover temperature and well within the transition region, broadened by the effects of finite size and finite quark mass. Thus, it appears difficult

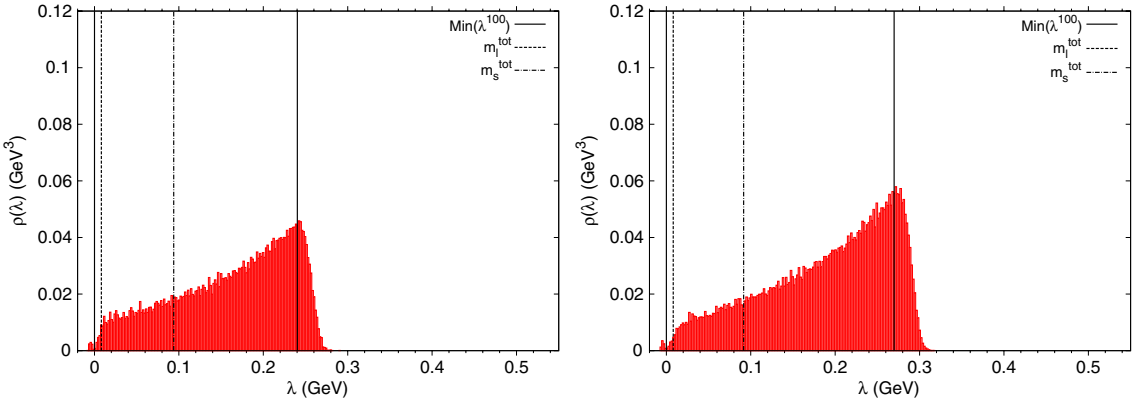

FIG. 12 (color online). Renormalized Dirac spectrum 149 MeV $L_s = 32$ (left) and 159 MeV (right).

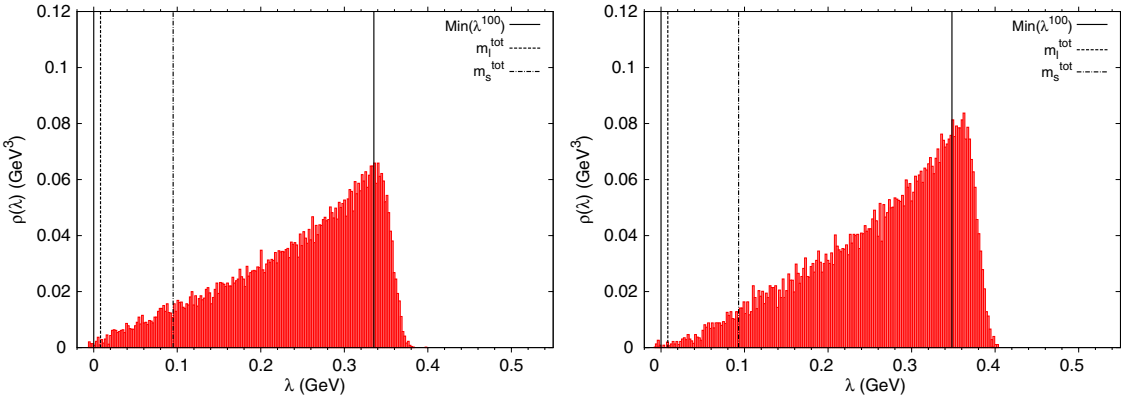

FIG. 13 (color online). Renormalized Dirac spectrum 168 MeV (left) and 177 MeV (right).

to determine the character of either $SU(2)_L \times SU(2)_R$ or $U(1)_A$ symmetry restoration at these temperatures without examining larger volumes and smaller quark masses.

For the temperatures $T = 168$ and 177 MeV the small λ behavior has qualitatively changed. The pronounced shoulder near $\lambda = 10$ MeV has disappeared and instead the spectral density is approaching zero in a more linear fashion. Looking carefully at the region $\lambda \approx 0$ for $T = 168$ MeV, one sees what appears to be essentially linear behavior as $\lambda \to 0$. At $T = 177$ MeV similar behavior can be seen, although because of our limited statistics, $\rho(\lambda)$ could vanish with a higher-than-linear power. For $T = 186$ MeV the behavior has changed again, with very few eigenvalues found below 20 MeV. At $T = 195$ MeV, where larger statistics better populate this interesting region, $\rho(\lambda)$ decreases to a minimum near 20 MeV and then increases to a peak near $\lambda = 0$.

This behavior at $T = 195$ MeV is consistent with that expected from the DIGA. However, integrating over this small peak for $\lambda \leq 20$ MeV and including those eigenvalues plotted to the left of zero, we find an average number of near-zero modes of 0.06/MeV. With such a low density of near-zero modes, we expect that the spectral broadening arising from the simultaneous presence of instantons and anti-instantons will be unimportant. Thus, it appears likely that the spread of eigenvalues about zero seen for $T = 195$ MeV is the result of finite lattice spacing. This conclusion is consistent with the approximately equal number of eigenvalues Λ slightly above $m_l + m_{\rm res}$ (giving $\lambda > 0$) and the number slightly below (giving λ imaginary) and plotted as $-|\lambda|$ to the left of zero. If this is correct, then we should expect that at $T = 195$ MeV and for a volume of spatial size $L \approx 2$ fm, $\rho(\lambda)$ will accurately approach a delta function, $\delta(\lambda)$ as $a \to 0$.

In summary, our study of the Dirac eigenvalue spectrum has provided limited but interesting results. For our $\approx$ 10 MeV quark mass and 2 fm spatial box, the transition region appears sufficiently broad that the spectral density found at $T = 149$ and 159 MeV is strongly influenced by finite volume effects. At $T = 168$ and 177 MeV interesting, possibly nonperturbative behavior is seen in the low-lying eigenvalue spectrum, $\rho(\lambda) \sim \lambda^\alpha$ with $\alpha \sim 1$–2, very different from the behavior of the free Dirac spectrum at finite temperature. Determining whether this behavior can support the breaking of $U(1)_A$ symmetry will require exploration with larger volumes and smaller masses.

Finally, a cluster of near-zero modes can be identified at the highest $T = 186$ and 195 MeV temperatures; see the insets in Fig. 14. Counting the number of near-zero modes in each of these clusters gives a density of zero modes of

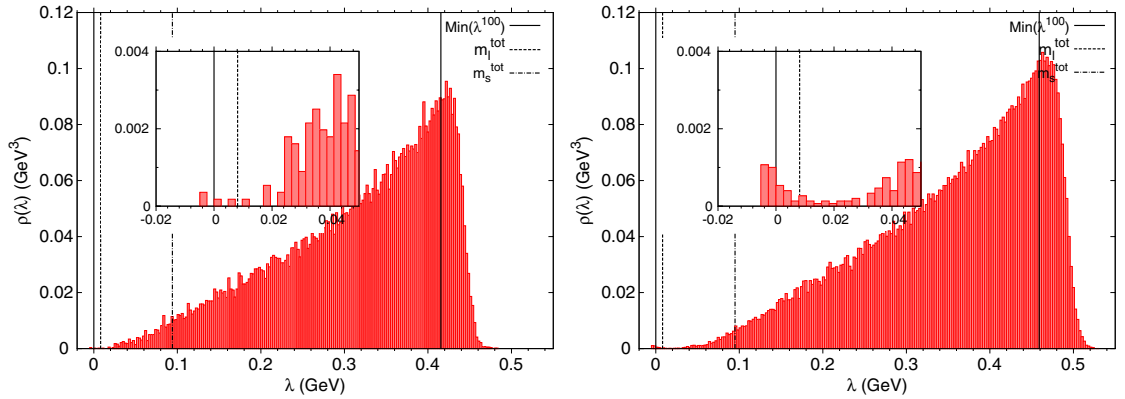

FIG. 14 (color online). Renormalized Dirac spectrum 186 MeV (left) and 195 MeV (right).

$0.0022(6)/\text{fm}^4$ and $0.0059(8)/\text{fm}^4$ for $T = 186$ and 195 MeV, respectively. If these near-zero modes can be described by a mass-dependent density of the DIGA form, $\rho(\lambda) = c_0 m^2 \delta(\lambda)$, then the densities found for $T = 186$ and 195 MeV can be used to determine values for c_0. Using Eq. (46), one can then calculate the resulting contributions to $(\chi_\pi - \chi_\delta)/T^2$, finding 6(2) and 17(2) for $T = 186$ and 195 MeV, respectively. These numbers compare reasonably well with the values of 6(2) and 8(4) determined directly from the integrated hadron correlators shown in Table XII.

2. Possible behaviors for $\rho(\lambda, m)$

Given the range of behaviors seen above for the function $\rho(\lambda)$ for T above the transition region, $T \geq 168$ MeV, it may be useful to discuss the consequences of possible functional forms of $\rho(\lambda, m)$ for the chiral condensate, the susceptibilities χ_π, χ_δ, their difference, $\chi_\pi - \chi_\delta$, and the disconnected chiral susceptibility χ_{disc}. In addition to the Banks-Casher relation given in Eq. (45), and Eq. (46) for the difference $\chi_\pi - \chi_\delta$, we can also relate χ_π to the eigenvalue density $\rho(\lambda)$ by inserting an eigenmode expansion in the expression for χ_π and obtain

$$\chi_\pi = \int_0^\infty d\lambda \rho(\lambda, m) \frac{2}{m^2 + \lambda^2} = \frac{\langle \bar{\psi}\psi \rangle}{m}. \tag{54}$$

Finally, the full chiral susceptibility $\chi_\sigma = \chi_{\text{con}} + \chi_{\text{disc}}$ is given by

$$\frac{\partial}{\partial m}\langle \bar{\psi}\psi \rangle = \int_0^\infty d\lambda \rho(\lambda, m) \frac{\partial}{\partial m}\left[\frac{2m}{m^2 + \lambda^2}\right] + \int_0^\infty d\lambda \frac{\partial}{\partial m}[\rho(\lambda, m)] \frac{2m}{m^2 + \lambda^2}, \tag{55}$$

$$\equiv \chi_{\text{con}} + \chi_{\text{disc}}. \tag{56}$$

We will now use these equations to determine the behavior of $\bar{\psi}\psi$, χ_π, χ_δ and χ_{disc} in the limit $m \to 0$ for three different assumed behaviors of $\rho(\lambda, m)$. The first is the behavior predicted by the DIGA, $\rho(\lambda, m) = C_0 m^2 \delta(\lambda)$. Next we consider the hypothesis that above T_c the density of eigenvalues is an analytic function of the quark mass and eigenvalue. To linear order, this gives two possible terms for $T \geq T_c$ since the constant term $\rho(0, 0)$ must vanish:

$$\rho(\lambda, m) = C_1 \lambda + C_2 m + O(\lambda m) + \cdots. \tag{57}$$

Table XIII lists the behavior for each of these four quantities that results from each Ansatz.

The Ansatz $\rho(\lambda, m) \propto \lambda$ yields a finite $\chi_\pi - \chi_\delta$ in the chiral limit. However, the mechanism by which it does so is somewhat unusual. The chiral condensate of this theory vanishes as $m \ln m$ in the chiral limit. The logarithm shows up as a divergence in the susceptibilities χ_π and χ_δ. However, it cancels out in the difference, leading to a finite $\chi_\pi - \chi_\delta$. Lastly, since there is no m dependence in the spectral density, the disconnected chiral susceptibility vanishes according to Eq. (56) and $\chi_\pi - \chi_\delta \neq \chi_{\text{disc}}$. As we have already seen in Eq. (39), the failure of this equality would imply the breaking of $SU(2)_L \times SU(2)_R$ symmetry for $T > T_c$.

TABLE XIII. Limiting behavior of various thermodynamic quantities as $m \to 0$ for three possible forms of $\rho(\lambda, m)$ for small m and λ. Note that the results in the right-hand columns have the correct multiplicative coefficients, given the Ansätze for $\rho(\lambda, m)$ in the leftmost column.

Ansatz	$\langle \bar{\psi}\psi \rangle$	χ_π	χ_δ	$\chi_\pi - \chi_\delta$	χ_{disc}
$m^2\delta(\lambda)$	m	1	-1	2	2
λ	$-2m\ln(m)$	$-2\ln(m)$	$-2\ln(m)$	2	0
m	πm	π	0	π	π

By contrast, the Ansatz $\rho(\lambda, m) \propto m$ does not give rise to logarithmic divergences. The chiral condensate vanishes linearly in the quark mass, the susceptibilities χ_π and $\chi_\pi - \chi_\delta$ both remain finite and furthermore $\chi_\pi - \chi_\delta = \chi_{\text{disc}}$ as well. Interestingly however, the susceptibility χ_δ vanishes in the chiral limit. The equality $\chi_\pi - \chi_\delta = \chi_{\text{disc}}$ is therefore just the equality $\chi_\pi = \chi_{\text{disc}}$.

The contrasting possibilities shown in Table XIII suggest that future studies of these susceptibilities in the limit of small quark mass will also reveal which of these behaviors for $\rho(\lambda, m)$ is present and the underlying mechanism of $U(1)_A$ symmetry breaking as a function of temperature for $T \geq T_c$.

Complications from limited statistics, distortion of the small eigenvalue spectrum caused by lattice artifacts, and the fact that we have examined only a single light-quark mass limit our ability to test for the behaviors compared in Table XIII in the present calculation. As noted above we do see evidence for the near-zero mode contributions described in the first row of Table XIII and rough consistency between these spectral results and the values of $\chi_\pi - \chi_\delta$ obtained from the integrated hadron correlators. It is also tempting to compare the apparent linear behavior of $\rho(\lambda)$, seen with the least ambiguity at $T = 168$ MeV, with the expectations from Table XIII. We find the coefficient c_1 in Eq. (57) to have the value $(362(12)\ \text{MeV})^2$ This results in a contribution 9(1) to $(\chi_\pi - \chi_\delta)/T^2$ at $T = 168$ MeV, compared with 36(14) obtained from direct integration of the relevant hadronic correlators. [Note that the value of $(362(12)\ \text{MeV})^2$ is much too large to be explained as an effect of explicit chiral symmetry breaking which should be on the order of $c_1 \approx (m + m_{\text{res}})\Lambda_{\text{QCD}} \approx (10\ \text{MeV}) \times (300\ \text{MeV})$, roughly 30 times too small.]

VII. CONCLUSION

The finite temperature properties of QCD are immediately accessible to standard, Euclidean-space calculations in lattice QCD. In fact, lattice QCD has provided valuable,

ab initio information and insights into QCD thermodynamics since its inception. However, the need to work in the large-volume, thermodynamic limit makes this a challenging application for lattice methods. The needed large physical volumes are achieved by working at relatively large lattice spacing, making QCD thermodynamics calculations especially vulnerable to finite lattice spacing errors and restricting the range of lattice spacings available to carry out a reliable continuum limit. As a result, it is important to examine the thermodynamic properties of QCD using a variety of lattice actions, as the effects of lattice discretization errors are likely to vary between different choices of lattice action.

An appealing fermion action to use when studying the QCD chiral phase transition is the domain wall action which accurately respects the chiral symmetry whose vacuum breaking and restoration drives this transition. Unfortunately, the large lattice spacings which are needed for thermodynamics studies are a special problem for the domain wall formulation where the rough gauge fields characteristic of large lattice spacing induce sizable explicit chiral symmetry breaking unless the size of the fifth dimension is made very large. As a result, earlier studies of QCD thermodynamics using domain wall fermions [27,28] have been compromised by the resulting large residual chiral symmetry-breaking effects. Because the residual chiral symmetry breaking increases at the larger lattice spacing associated with lower temperatures, these effects can potentially distort the observed temperature dependence seen in the transition region.

In the calculation reported here, we have succeeded in controlling these effects. First we have shown results from a brute force approach using a very large fifth-dimensional extent of $L_s = 96$. Second, we have employed the carefully tuned DSDR gauge action where the short-distance structure has been chosen to suppress the gauge-field dislocations which induce explicit chiral symmetry breaking. As a result, we are able to report a systematic study of the transition region on a line of constant physics with a pion mass of 200 MeV. This has been achieved using the DSDR gauge action, $L_s = 32$ or 48 and a small input bare quark mass which varies from positive to negative as the temperature is decreased below 159 MeV.

Using this chirally symmetric lattice fermion formulation we have been able to confirm the expected chiral behavior of the QCD phase transition seen using staggered fermions. Specifically, in a lattice formulation with three degenerate light pions of fixed physical mass possessing the $SU(2)_L \times SU(2)_R$ chiral symmetry found in Nature, we see a crossover behavior going from the low-temperature region, $T \leq 159$ MeV, with vacuum chiral symmetry breaking to a chirally symmetric phase at higher temperature, $T \geq 168$ MeV, in which the large, low-temperature chiral condensate has dramatically decreased and the spatial Green's functions and screening lengths show good chiral symmetry.

We have explored this phenomena microscopically by examining the spectrum of the fermion Dirac operator, normalized using standard $\overline{\text{MS}}$ conventions. We find the expected nonzero eigenvalue density for small eigenvalues at low temperature required by vacuum chiral symmetry breaking and the Banks-Casher relation. As the temperature increases, this density at small eigenvalue decreases dramatically until $T = 186$ and 195 MeV where we find a striking absence of small eigenvalues. In fact, except for a small density near zero, which may be attributed to semiclassical instanton effects, one might identify a gap in the spectrum below 20 MeV at these two highest temperatures. In the important region closer to T_c, $159\ \text{MeV} < T < 177\ \text{MeV}$, the behavior of the eigenvalue spectrum remains uncertain. While one might assign linear behavior, $\rho(\lambda) \propto \lambda$, at small λ to the $T = 168$ MeV spectrum shown in Fig. 13, the picture could also change dramatically with increased volume.

Of particular interest in the current study is the degree to which the anomalous $U_A(1)$ symmetry is found to be broken at high temperature. For temperatures below the chiral transition, both the anomalous and nonanomalous axial symmetries are broken by the vacuum, making the effects of the axial anomaly difficult to see. (Only the relatively heavy η' meson stands out at low energy as a consequence of the axial anomaly.) However, above the QCD phase transition, the three nonanomalous axial symmetries are explicitly realized in a Wigner mode and the effects of the axial anomaly on the potential $U_A(1)$ symmetry can be easily explored. We find rapidly decreasing $U(1)_A$-breaking susceptibilities and susceptibility differences with increasing temperature. Our results at the two highest temperatures of 186 and 195 MeV are consistent with a picture in which $U(1)_A$ symmetry is largely realized with the small remaining asymmetries appearing to arise from relatively rare gauge-field configurations carrying nontrivial topology. The dearth of small Dirac eigenvalues at high temperatures mentioned above supports this picture of effective $U_A(1)$ symmetry restoration.

It should be emphasized that the calculations reported here have been carried out on a relative small, $16^3 \times 8$ physical volume. This aspect ratio of spatial to temporal size of 2 is much smaller than that in the typical staggered fermion calculation and introduces important uncertainties in our results. While the disconnected chiral susceptibility as a function of temperature shown in Fig. 7 shows interesting deviations from the results in earlier staggered work, we expect that at least part of this difference is caused by our small lattice volume. Fortunately, while calculations on larger spatial volumes are difficult when using the five-dimensional DWF formulation, the scale of computer resources now becoming available for these calculations will allow an increase in lattice volume from the present 16^3 to 32^3 and 48^3. Thus, over the next one to two years, the methods introduced and demonstrated here can be used to

study appropriately large volumes allowing both a careful comparison with earlier staggered fermion results and important exploration of those symmetry and spectral properties which are best examined with a chiral fermion formulation.

ACKNOWLEDGMENTS

This work has been supported in part by Contracts No. DE-AC02-98CH10886, No. DE-AC52-07NA27344, No. DE-FC06-ER41446, No. DE-FG02-92ER40699, No. DE-FG02-91ER-40628, No. DE-FG02-91ER-40661, No. DE-FG02-04ER-41298, No. DE-KA-14-01-02 with the U.S. Department of Energy, Lawrence Livermore National Laboratory under Contract No. DE-AC52-07NA27344, NSF Grants No. PHY0903571, No. PHY08-57333, No. PHY07-57035, No. PHY07-57333, and No. PHY07-03296. N. C., Z. L., R. M., and H. Y. were supported in part by U.S. DOE Grant No. DE-FG02-92ER40699. The numerical calculations have been performed on the QCDOC computers of the RIKEN BNL Reseach Center, the BlueGene/L and BlueGene/P computers at Lawrence Livermore National Laboratory (LLNL) and the New York Center for Computational Sciences (NYCCS) at Brookhaven National Laboratory. We thank the LLNL Multiprogrammatic and Institutional Computing program for time on the LLNL BlueGene/L and BlueGene/P supercomputer.

APPENDIX A: NORMALIZATION OF DWF DIRAC SPECTRUM

In this Appendix we repeat the arguments of Giusti and Lüscher [30] to demonstrate that Dirac eigenvalue density $\rho(\lambda)$ has a scheme-dependent continuum limit which transforms under a change of conventions as shown in Eq. (7). Using these methods we then determine how such a "physical" spectral density, $\rho(\lambda)$, can be determined from the eigenvalue distribution found for the DWF Dirac operator.

Following Giusti and Lüscher we consider a single flavor of fermion with field variables $q(x)$ and $\bar{q}(x)$ which in a continuum formulation would have the Euclidean action density $\bar{q}(x)(\gamma^\nu D_\nu + m)q(x)$. This single fermion flavor is then replicated, creating k doublet fields $q^j(x)$ and $\bar{q}^j(x)$, $1 \le j \le k$. Finally a twisted-mass term is added to the continuum action giving

$$\mathcal{L}(x) = \sum_{j=1}^{k} \bar{q}^j(x)(\gamma^\nu D_\nu + m + i\mu\gamma^5\tau^3)q^j(x), \tag{A1}$$

where τ^3 is one of the standard Pauli matrices τ^i acting on the implicit doublet degrees of freedom of $q^j(x)$.

This generalized action is then used to define the Green's function

$$\sigma_3(\mu) = -\prod_{n=1}^{6}\langle P^+_{1,2}(x_1)P^-_{2,3}(x_2)P^+_{3,4}(x_3)P^-_{4,5}(x_4) \times P^+_{5,6}(x_5)P^-_{6,1}(x_6)\rangle, \tag{A2}$$

where $P^\pm_{ll'} = (P^1_{ll'} \pm P^2_{ll'})/2$ and the operators $P^i_{ll'}$ are defined by

$$P^i_{ll'} = \bar{q}^l(x)\tau^i q^{l'}(x). \tag{A3}$$

The Green's function given in Eq. (A2) can be defined for the case of six doublets, $k = 6$, and can easily be generalized to define $\sigma_{k/2}(\mu)$. The structure of Eq. (A2) ensures that the fermions flow in a single loop constructed from the product of six fermion propagators which can be evaluated directly in QCD perturbation theory. The brackets $\langle\cdots\rangle$ in Eq. (A2) describe the gauge average appropriate to the original theory. Thus, no fermion determinant should be introduced for any of the k fermion fields appearing in these Green's functions.

By design, the Green's function defined in Eq. (A2) also can be written as a path integral over the gauge degrees of freedom of a product of fermion propagators, evaluated in each gauge background:

$$\sigma_3(\mu) = \left\langle \mathrm{tr}\left\{\frac{1}{((\gamma^5 D)^2 + \mu^2)^3}\right\}\right\rangle, \tag{A4}$$

where $\gamma^5 D = \gamma^5\gamma^\nu D_\nu + \gamma^5 m$ is the Hermitian Euclidean Dirac operator and the γ^5 matrices which appear in the vertex operators $P^\pm_{ll'}$ have been combined into the operators appearing in the propagators resulting in the simple trace of products shown in Eq. (A4).

Finally, the connection between $\sigma_3(\mu)$ and the eigenvalue density $\rho(\lambda)$ can established if, for each gauge configuration in the average appearing in Eq. (A4), we evaluate the trace of products of Dirac propagators in the basis of eigenstates of the Hermitian Dirac operator $\gamma^5 D$:

$$\sigma_3(\mu) = \left\langle \sum_n \frac{1}{(\lambda_n^2 + \mu^2)^3}\right\rangle \tag{A5}$$

$$= \int_{-\infty}^{\infty} d\lambda \rho(\lambda)\frac{1}{(\lambda^2 + \mu^2)^3}, \tag{A6}$$

where the λ_n are the eigenvalues of $\gamma^5 D$ on each gauge configuration over which the average is being performed. In the final step we have made the usual replacement,

$$\sum_n f(\lambda_n) = \int_{-\infty}^{\infty} d\lambda\left(\sum_n \delta(\lambda - \lambda_n)\right) f(\lambda), \tag{A7}$$

for an arbitrary function $f(\lambda)$ and adopted the usual definition,

$$\rho(\lambda) = \left\langle \sum_n \delta(\lambda - \lambda_n)\right\rangle. \tag{A8}$$

The transform given in Eq. (A6) determining $\sigma_3(\mu)$ in terms of $\rho(\lambda)$ can be inverted, allowing $\rho(\lambda)$ to be defined from the Green's function $\sigma_3(\mu)$. Since the operators $P^\pm_{ll'}$

and the related twisted-mass term $\bar{q}\gamma^5\tau^3 q$ can be given a meaning in the continuum limit, $\sigma_3(\mu)$ and hence $\rho(\lambda)$ can be defined in the continuum limit as well. If we work with a second regularization scheme, the corresponding mass operators $P'^{\,i}_{ll'}$ will have long-distance matrix elements related to those of the first scheme by

$$P'^{ii}_{ll'} = \frac{1}{Z_{m\to m'}} P^i_{ll'}. \tag{A9}$$

We can exploit this equation to relate the corresponding Green's functions $\sigma'_3(\mu)$ and $\sigma_3(\mu)$:

$$\sigma'_3(\mu') = \frac{1}{(Z_{m\to m'})^6}\sigma_3(\mu'/Z_{m\to m'}), \tag{A10}$$

which in turn implies that $\rho'(\lambda')$ and $\rho(\lambda)$ are related by Eq. (7).

We can now easily generalize this approach to the case of domain wall fermions. We need only identify three operators which are the DWF analogue of the $P^i_{ll'}$ defined above. Since the product of the usual DWF Dirac operator D^{DWF} with γ^5 and the reflection operator R_5 defined in Sec. III is Hermitian, we define

$$P^{\mathrm{DWF},i}_{ll'}(x) = \sum_{s=0}^{L_s-1} \bar{\Psi}_l(x,s)\gamma^5\tau^i\Psi_{l'}(x,L_s-1-s), \tag{A11}$$

where, as above, we have introduced k doublet five-dimensional fields $\Psi_l(x)$, $1 \le l \le k$ in precise analogy with the generic treatment of Giusti and Lüscher above. As above we can use $P^{\mathrm{DWF},i}_{ll'}(x)$ to define a corresponding Green's function $\sigma_3^{\mathrm{DWF}}(\mu)$ which, as above, is directly related to the spectrum of DWF Dirac eigenvalues which we can obtain by numerically diagonalizing $D^{\mathrm{DWF}}\gamma^5 R_5$. Again, as above, we can relate this spectrum to the Dirac spectrum found in a different lattice regularization or in a continuum scheme if we determine the needed normalization factor Z_{tw} connecting the operators $P^{\mathrm{DWF},i}_{ll'}(x)$ and those for the second scheme.

APPENDIX B: RENORMALIZATION OF STAGGERED CHIRAL SUSCEPTIBILITIES

In order to compare the chiral susceptibility between the DWF and staggered actions, we must also calculate the renormalization factors for the HISQ and asqtad actions used in [59]. The ensembles used in that work lie on slightly different lines of constant physics, given by $m_\pi r_0 = 0.381$ and $m_\pi r_0 = 0.425$ for the HISQ and asqtad actions, respectively. This corresponds to $m_\pi = 161$ MeV and $m_\pi = 179$ MeV if one converts to physical units using $r_0 = 0.468$ fm, the value for the Sommer parameter determined from staggered calculations. Using the $\overline{\mathrm{MS}}$ masses $m_l = 3.2(2)$ MeV and $m_s = 88(5)$ MeV at $\mu = 2$ GeV determined in [69], we can calculate the renormalization factors necessary to convert to $\overline{\mathrm{MS}}$ scheme:

$$Z_m = \frac{91.2\ \mathrm{MeV}}{2\tilde{m}}\left(\frac{m_\pi}{495\ \mathrm{MeV}}\right)^2. \tag{B1}$$

The renormalized, one-flavor susceptibility is then given by

$$\chi^{\mathrm{renorm}}_{1f}/T^2 = \frac{1}{4}\left(\frac{1}{Z_{m_f\to\overline{\mathrm{MS}}}(\mu^2)}\right)^2 \chi^{\mathrm{bare}}_{2f}/T^2, \tag{B2}$$

where $\chi^{\mathrm{bare}}_{2f}$ is the bare two-flavor susceptibility tabulated in [59], and the factor of $1/4$ in Eq. (B2) converts to the one-flavor normalization used in this work.

APPENDIX C: RATIONAL HYBRID MONTE CARLO (RHMC) ENSEMBLE GENERATION ALGORITHMS

Here we give a brief description of the specific evolution algorithms used to generate the DSDR gauge-field ensembles used in this paper. Recall that these ensembles are generated using the Iwasaki gauge action, the DSDR action formed from the ratio of twisted-mass Wilson determinants given in Eq. (3) and the ratio of the DWF determinants for two flavors of light quarks with mass m_l and one strange quark flavor with mass m_s divided by three corresponding DWF Pauli-Villars determinants with mass $m_f = 1$. These DWF determinants are constructed from the following ingredients.

A quotient fermion action is derived from the following fermion determinant:

$$\det\left(\frac{M^\dagger(m)M(m)}{M^\dagger(1)M(1)}\right) = \int \mathcal{D}\phi^\dagger\mathcal{D}\phi\,\exp\left(-\phi^\dagger M(1)\frac{1}{M^\dagger(m)M(m)}M^\dagger(1)\phi\right), \tag{C1}$$

where M is the five-dimensional DWF Dirac operator. The Hasenbusch factorization [70] rewrites the above quotient action as a product of quotient actions by introducing k intermediate masses,

$$\det\left(\frac{M^\dagger(m)M(m)}{M^\dagger(1)M(1)}\right) = \prod_{i=1}^{k+1}\det\left(\frac{M^\dagger(m_{i-1})M(m_{i-1})}{M^\dagger(m_i)M(m_i)}\right) \tag{C2}$$

$$= \prod_{i=1}^{k+1}\int \mathcal{D}\phi_i^\dagger\mathcal{D}\phi_i \times \exp\left(-\phi_i^\dagger M(m_i)\frac{1}{M^\dagger(m_{i-1})M(m_{i-1})}M^\dagger(m_i)\phi_i\right), \tag{C3}$$

where $m = m_0 < m_1 < \cdots < m_{k+1} = 1$.

In the following the symbol $S_{\mathrm{Q}}(m_1,m_2)$ is used to represent the quotient fermion action,

$$S_{\mathrm{Q}}(m_1,m_2) = \phi^\dagger M(m_2)\frac{1}{M^\dagger(m_1)M(m_1)}M^\dagger(m_2)\phi, \tag{C4}$$

TABLE XIV. Scheme 1 with a total of $N = 4$ levels of nested integrators. The quotient action $S_Q(m_l, 1)$ is split into $S_Q(m_l, 0.01) + S_Q(0.01, m_s) + S_R(m_s, 1) + S_R(m_s, 1)$. Note that two copies of the rational action $S_R(m_s, 1)$ are used to replace a single quotient action $S_Q(m_s, 1)$. Ensembles 4 (159 MeV), 5 (168 MeV), 6 (177 MeV), and 7 (186 MeV) were generated using this scheme, using top level step size 1/4. The light and strange quark masses m_l and m_s can be found in Table II.

Level (i)	S_i	Integrator type	n_i
1	$S_Q(m_l, 0.01) + S_Q(0.01, m_s)$	Omelyan QPQPQ	1
2	$S_R(m_s, 1) + S_R(m_s, 1) + S_R(m_s, 1)$	Omelyan QPQPQ	4
3	S_{DSDR}	Omelyan QPQPQ	6
4	S_G	Omelyan QPQPQ	1

where Q means "quotient". Note that each quotient action has a different pseudofermion field ϕ. This fact is not represented in Eq. (C4).

The quotient action discussed above accounts for two degenerate sea quarks. This is used to simulate the two light quarks in the hybrid Monte Carlo algorithm. For simulating the strange quark, the rational approximation needs to be used:

$$\det\left(\frac{M^\dagger(m)M(m)}{M^\dagger(1)M(1)}\right)^{1/2} = \int \mathcal{D}\phi^\dagger \mathcal{D}\phi \exp\Big(-\phi^\dagger (M^\dagger(1)M(1))^{1/4} \times \frac{1}{(M^\dagger(m)M(m))^{1/2}} (M^\dagger(1)M(1))^{1/4}\phi\Big), \quad \text{(C5)}$$

where rational approximations to $x^{1/4}$ and $x^{-1/2}$ are used to evaluate the noninteger powers of these matrices. In the following, the symbol $S_R(m_1, m_2)$ is used to represent this rational action,

$$S_R(m_1, m_2) = \phi^\dagger (M^\dagger(m_2)M(m_2))^{1/4} \frac{1}{(M^\dagger(m_1)M(m_1))^{1/2}} \times (M^\dagger(m_2)M(m_2))^{1/4}\phi, \quad \text{(C6)}$$

where fractional powers such as $x^{1/4}$ and $x^{-1/2}$ are understood to be shorthand notations for their corresponding rational approximations. The "R" in S_R means "rational".

The final Hamiltonian used in the RHMC evolution contains the following parts:

$$H = T(p) + S_G + S_{DSDR} + S_R(m_s, 1) + S_Q(m_l, 1). \quad \text{(C7)}$$

Here S_G and S_{DSDR} represent the gauge action and the DSDR action, while $T(p)$ is the kinetic term. We split $S_Q(m_l, 1)$ into a few quotient actions using the Hasenbusch factorization as in Eqs. (C2) and (C3). A single quotient action can also be replaced by two rational actions given in Eq. (C5) using the "Nroots" acceleration method.

When evolving the above action, we use multiple levels of nested integrators to separate different parts of the action. At each level we use an Omelyan QPQPQ or force gradient QPQPQ integrator. A general multilevel Sexton-Weingarten integration scheme can be written as follows:

$$H = T'_0 = T'_1 + S_1, \quad \text{(C8)}$$

$$T'_i = T'_{i+1} + S_{i+1} \qquad i = 1, 2, \ldots, N-1, \quad \text{(C9)}$$

where T'_i, $i = 0, 1, N-1$ is the Hamiltonian to be integrated at level i. The ith-level Hamiltonian T'_i is further split into T'_{i+1} and S_i, which are the Q and P parts used by the Omelyan or force gradient integrator. The Hamiltonian T'_N at the last level is the kinetic term $T(p)$. The above equations separate the entire action into N levels.

The details of the RHMC algorithms used in this paper are listed in Tables XIV and XV. The column labeled level (i) in these tables contains the integer n_i which specifies the number of T' steps in the Sexton-Weingarten integration

TABLE XV. Scheme 2 with a total of $N = 3$ levels of nested integrators. Ensemble 1 (139 MeV), 2 and 3 (149 MeV), and 8 (195 MeV) were generated using this scheme. Ensembles 1, 2, and 3 used the force gradient QPQPQ integrator [74] with top level step size 1/7, while 8 used the Omelyan QPQPQ integrator with top level step size 1/8. Here m_i, $i = 0, 1, \ldots, 6$, represent different Hasenbusch masses, with $m_0 = m_l$, $m_1 = 0.01$, $m_2 = 0.06$, $m_3 = 0.18$, $m_4 = 0.37$, $m_5 = 0.67$ and $m_6 = 1$. The masses m_l and m_s can be found in Table II.

Level (i)	S_i	Integrator type	n_i
1	$\sum_{i=1}^{6} S_Q(m_{i-1}, m_i) + S_R(m_s, 1)$	Omelyan/FG QPQPQ	4
2	S_{DSDR}	Omelyan/FG QPQPQ	1
3	S_G	Omelyan/FG QPQPQ	1

scheme for each level while S_i specifies the part of the action in Eq. (C7) included in each level.

APPENDIX D: COMPARISON OF χ_{top} AND $\chi_{\text{5,disc}}$

In this Appendix we investigate the large discrepancy between the topological susceptibility χ_{top} and the pseudoscalar susceptibility $m_{l,\text{tot}}^2\chi_{5,\text{disc}}$ shown in Fig. 9 and described in Sec. VI A. The relation between χ_{top} and $m_{l,\text{tot}}^2\chi_{5,\text{disc}}$ given in Eq. (43) is often viewed as providing a good definition of χ_{top} since the fermionic quantity has a better understood continuum limit [30,71–73]. However, we compute χ_{top} using a widely used method which usually gives consistent results so the discrepancy found here caused us to look carefully at our code and to seek further tests of our results for both χ_{top} and $\chi_{5,\text{disc}}$.

For both quantities our computational procedures appear to be robust. We increased the number of random sources used to determine $\chi_{5,\text{disc}}$ from ten to 100 and saw only the expected decease in statistical errors. Independent code gave consistent results. We increased the number of smearing steps performed before the determination of χ_{top} from 60 to 150 and saw no systematic change in the result.

We cannot make a meaningful comparison of the relationship given in Eq. (42) on individual configurations because at least the right side of this relation takes on its continuum meaning only after a gauge average is performed. Because both sides are parity odd, a gauge average will give a nonzero result only if the equation is squared, leading us back to the relation we are trying to test. However, more information can be obtained by examining other products of similar parity-odd operators. Specifically, we examine χ_{top} and the four additional quantities:

$$X_l = m_{l,\text{tot}}^2\chi_{l,\text{disc}}^5, \tag{D1}$$

$$X_s = \frac{1}{V}m_{s,\text{tot}}^2\left\langle\left(\int d^4x\,\bar{\psi}_s(x)\gamma^5\psi_s(x)\right)\times\left(\int d^4y\,\bar{\psi}_s(y)\gamma^5\psi_s(y)\right)\right\rangle, \tag{D2}$$

$$X_{l,s} = \frac{1}{V}m_{l,\text{tot}}m_{s,\text{tot}}\left\langle\left(\int d^4x\,\bar{\psi}_l(x)\gamma^5\psi_l(x)\right)\times\left(\int d^4y\,\bar{\psi}_s(y)\gamma^5\psi_s(y)\right)\right\rangle, \tag{D3}$$

$$X_{l,\text{top}} = \frac{1}{V}m_{l,\text{tot}}\left\langle\left(\int d^4x\,\bar{\psi}_l(x)\gamma^5\psi_l(x)\right)(Q_{\text{top}})\right\rangle, \tag{D4}$$

TABLE XVI. Results for five different susceptibilities computed on both finite and zero-temperature ensembles. All the values are given in lattice units with a factor of 10^{-6} removed.

#	T (MeV)	X_l	X_s	$X_{l,s}$	χ_{top}	$X_{l,\text{top}}$
1	139	36(3)	51(20)	42(5)	107(5)	37(3)
2	149	27(3)	35(20)	29(4)	54(2)	26(2)
3	149	31(2)	44(19)	33(4)	57(2)	30(2)
4	159	16(2)	6(12)	15(3)	27(2)	15(2)
5	168	9(2)	−11(12)	6(2)	15(2)	9(2)
6	177	5(1)	−1(8)	4(2)	7.6(9)	4.8(8)
7	186	1.7(7)	−3(6)	1(1)	4(1)	2.0(8)
8	195	1.4(5)	4(7)	1.3(9)	2.2(5)	1.5(5)
10	···	50(9)	67(22)	55(12)	49(7)	44(8)
11	···	54(8)	33(56)	43(16)	62(6)	47(6)
15	···	20(3)	2(20)	16(53)	23(4)	21(4)

all five of which should agree. The results are shown in Table XVI.

While the errors on the strange quark susceptibilities X_s are too large to allow a meaningful test, the light-quark susceptibilities X_l and the light-strange product $X_{l,s}$ agree within their 10% to 20% errors. This reaffirms the consistency of the results computed directly from the fermion fields and supports the view that the fermionic quantities, which are the basis of most of the results in this paper, are behaving as expected. Note, this includes the interpretation of the total bare quark mass as the sum of the input plus the residual mass $m_f + m_{\text{res}}$ since the ratio of m_{res} to m_f various substantially among the rows in Table XVI. However, those susceptibilities are much smaller than χ_{top} at temperatures near or below the transition region (see also Fig. 9). This discrepancy is not visible at higher temperatures or for the zero-temperature ensembles.

The rightmost column in Table XVI offers some insight into this discrepancy. Comparing the X_l and $X_{l,\text{top}}$ columns shows agreement between the pure fermionic susceptibility X_l and the cross, fermion-topological susceptibility $X_{l,\text{top}}$ within their 10% to 20% errors for all the ensembles. This suggests the presence of unphysical fluctuations in the gauge-field observable Q_{top} at lower temperatures. These unphysical fluctuations are uncorrelated with the fermionic degrees of freedom and hence do not pollute the cross correlator $X_{l,\text{top}}$. However, they do add to the fluctuations in Q_{top}, leading to an unphysical increase in χ_{top}. At $T =$ 140 MeV these unphysical fluctuations appear to have the same size as those which are physical.

[1] S. L. Adler, Phys. Rev. **177**, 2426 (1969).
[2] J. S. Bell and R. Jackiw, Nuovo Cimento A **60**, 47 (1969).
[3] G. 't Hooft, Phys. Rev. Lett. **37**, 8 (1976).
[4] D. B. Kaplan, Phys. Lett. B **288**, 342 (1992).
[5] V. Furman and Y. Shamir, Nucl. Phys. **B439**, 54 (1995).
[6] S. Durr and C. Hoelbling, Phys. Rev. D **71**, 054501 (2005).
[7] S. Durr, Proc. Sci., LAT2005 (2006) 021.
[8] S. R. Sharpe, Proc. Sci., LAT2006 (2006) 022.
[9] G. C. Donald, C. T. Davies, E. Follana, and A. S. Kronfeld, Phys. Rev. D **84**, 054504 (2011).
[10] D. H. Adams, Phys. Rev. Lett. **104**, 141602 (2010).
[11] D. J. Gross, R. D. Pisarski, and L. G. Yaffe, Rev. Mod. Phys. **53**, 43 (1981).
[12] R. D. Pisarski and F. Wilczek, Phys. Rev. D **29**, 338 (1984).
[13] A. Butti, A. Pelissetto, and E. Vicari, J. High Energy Phys. 08 (2003) 029.
[14] F. Basile, A. Pelissetto, and E. Vicari, Proc. Sci., LAT2005 (**2006**) 199.
[15] R. Rapp and J. Wambach, Adv. Nucl. Phys. **25**, 1 (2000).
[16] E. V. Shuryak, Comments Nucl. Part. Phys. **21**, 235 (1994).
[17] Z. Huang and X.-N. Wang, Phys. Rev. D **53**, 5034 (1996).
[18] J. I. Kapusta, D. Kharzeev, and L. D. McLerran, Phys. Rev. D **53**, 5028 (1996).
[19] T. Csorgo, R. Vertesi, and J. Sziklai, Phys. Rev. Lett. **105**, 182301 (2010).
[20] P. Petreczky, J. Phys. G **39**, 093002 (2012).
[21] S. Mukherjee, J. Phys. G **38**, 124022 (2011).
[22] C. W. Bernard, T. Blum, C. E. Detar, S. A. Gottlieb, U. M. Heller, J. Hetrick, K. Rummukainen, R. Sugar, D. Toussaint, and M. Wingate, Phys. Rev. Lett. **78**, 598 (1997).
[23] S. Chandrasekharan, D. Chen, N. H. Christ, W.-J. Lee, R. Mawhinney, and P. Vranas, Phys. Rev. Lett. **82**, 2463 (1999).
[24] J. Kogut, J. Lagae, and D. Sinclair, Phys. Rev. D **58**, 054504 (1998).
[25] M. Cheng, S. Datta, A. Francis, J. van der Heide, C. Jung *et al.*, Eur. Phys. J. C **71**, 1564 (2011).
[26] H. Ohno, U. Heller, F. Karsch, and S. Mukherjee, Proc. Sci., LATTICE2011 (2011) 210.
[27] P. Chen *et al.*, Phys. Rev. D **64**, 014503 (2001).
[28] M. Cheng, N. H. Christ, M. Li, R. D. Mawhinney, D. Renfrew, F. Karsch, M. Lin, and P. Vranas, Phys. Rev. D **81**, 054510 (2010).
[29] S. Borsanyi, Y. Delgado, S. Durr, Z. Fodor, S. Katz *et al.*, Phys. Lett. B **713**, 342 (2012).
[30] L. Giusti and M. Luscher, J. High Energy Phys. 03 (2009) 013.
[31] P. de Forcrand, M. Garcia Perez, and I.-O. Stamatescu, Nucl. Phys. **B499**, 409 (1997).
[32] D. J. Antonio *et al.* (RBC Collaboration and UKQCD Collaboration), Phys. Rev. D **77**, 014509 (2008).
[33] P. M. Vranas, arXiv:hep-lat/0001006.
[34] P. M. Vranas, Phys. Rev. D **74**, 034512 (2006).
[35] H. Fukaya, S. Hashimoto, K.-I. Ishikawa, T. Kaneko, H. Matsufuru, T. Onogi, and N. Yamada (JLQCD Collaboration), Phys. Rev. D **74**, 094505 (2006).
[36] Y. Iwasaki, Report No. UTHEP-118, 1983.
[37] D. Antonio *et al.* (RBC and UKQCD Collaborations), Phys. Rev. D **75**, 114501 (2007).
[38] C. Allton *et al.* (RBC and UKQCD Collaborations), Phys. Rev. D **76**, 014504 (2007).
[39] C. Allton *et al.* (RBC-UKQCD Collaboration), Phys. Rev. D **78**, 114509 (2008).
[40] Y. Aoki *et al.* (RBC Collaboration and UKQCD Collaboration), Phys. Rev. D **83**, 074508 (2011).
[41] D. Renfrew, T. Blum, N. Christ, R. Mawhinney, and P. Vranas, Proc. Sci., LATTICE2008 (**2008**) 048.
[42] T. Blum, P. Boyle, N. Christ, N. Garron, E. Goode *et al.*, Phys. Rev. Lett. **108**, 141601 (2012).
[43] C. Kelly, Proc. Sci., LATTICE2011 (**2011**) 285 [arXiv:1201.0706].
[44] M. Golterman and Y. Shamir, Phys. Rev. D **68**, 074501 (2003).
[45] M. Golterman, Y. Shamir, and B. Svetitsky, Phys. Rev. D **71**, 071502 (2005).
[46] M. Golterman, Y. Shamir, and B. Svetitsky, Phys. Rev. D **72**, 034501 (2005).
[47] T. Blum, P. Chen, N. H. Christ, C. Cristian, C. Dawson *et al.*, Phys. Rev. D **69**, 074502 (2004).
[48] G. Martinelli, C. Pittori, C. T. Sachrajda, M. Testa, and A. Vladikas, Nucl. Phys. **B445**, 81 (1995).
[49] Y. Aoki *et al.*, Phys. Rev. D **78**, 054510 (2008).
[50] M. Gockeler, R. Horsley, H. Oelrich, H. Perlt, D. Petters, P. E. L. Rakow, A. Schäfer, G. Schierholz, and A. Schiller, Nucl. Phys. **B544**, 699 (1999).
[51] T. Kalkreuter and H. Simma, Comput. Phys. Commun. **93**, 33 (1996).
[52] G. Liu, Ph.D. thesis, Columbia University, 2003.
[53] S. H. Lee and T. Hatsuda, Phys. Rev. D **54**, R1871 (1996).
[54] N. J. Evans, S. D. Hsu, and M. Schwetz, Phys. Lett. B **375**, 262 (1996).
[55] M. C. Birse, T. D. Cohen, and J. A. McGovern, Phys. Lett. B **388**, 137 (1996).
[56] J. Engels, L. Fromme, and M. Seniuch, Nucl. Phys. **B675**, 533 (2003).
[57] T. Banks and A. Casher, Nucl. Phys. **B169**, 103 (1980).
[58] S. Chandrasekharan and N. H. Christ, Nucl. Phys. Proc. Suppl. **47**, 527 (1996).
[59] A. Bazavov, T. Bhattacharya, M. Cheng, C. DeTar, H. Ding *et al.*, Phys. Rev. D **85**, 054503 (2012).
[60] J. Braun, B. Klein, and P. Piasecki, Eur. Phys. J. C **71**, 1576 (2011).
[61] G. 't Hooft, Phys. Rev. D **14**, 3432 (1976).
[62] T. D. Cohen, arXiv:nucl-th/9801061.
[63] M. Albanese *et al.* (APE Collaboration), Phys. Lett. B **192**, 163 (1987).
[64] M. Gockeler, H. Hehl, P. E. Rakow, A. Schafer, W. Soldner, and T. Wettig, Nucl. Phys. Proc. Suppl. **94**, 402 (2001).
[65] P. Damgaard, U. M. Heller, R. Niclasen, and K. Rummukainen, Nucl. Phys. **B583**, 347 (2000).
[66] R. V. Gavai, S. Gupta, and R. Lacaze, Phys. Rev. D **65**, 094504 (2002).
[67] R. Gavai, S. Gupta, and R. Lacaze, Phys. Rev. D **77**, 114506 (2008).
[68] G. Cossu *et al.* (JLQCD Collaboration), Proc. Sci., LATTICE2010 (2010) 174.

[69] A. Bazavov, D. Toussaint, C. Bernard, J. Laiho, C. DeTar *et al.*, Rev. Mod. Phys. **82**, 1349 (2010).
[70] M. Hasenbusch, Phys. Lett. B **519**, 177 (2001).
[71] L. Giusti, G. Rossi, and M. Testa, Phys. Lett. B **587**, 157 (2004).
[72] M. Luscher, Phys. Lett. B **593**, 296 (2004).
[73] M. Luscher and F. Palombi, J. High Energy Phys. 09 (2010) 110.
[74] A. Kennedy, M. Clark, and P. Silva, Proc. Sci., LAT2009 (2009) 021.